Solar Dynamo Theory

Paul Charbonneau

Département de Physique, Université de Montréal, Montréal, Québec H3T 1N8, Canada;
email: paulchar@astro.umontreal.ca

Keywords

Sun, magnetohydrodynamics, hydromagnetic dynamo, solar cycle, turbulent convection, differential rotation

Abstract

The Sun's magnetic field is the engine and energy source driving all phenomena collectively defining solar activity, which in turn structures the whole heliosphere and significantly impacts Earth's atmosphere down at least to the stratosphere. The solar magnetic field is believed to originate through the action of a hydromagnetic dynamo process operating in the Sun's interior, where the strongly turbulent environment of the convection zone leads to flow-field interactions taking place on an extremely wide range of spatial and temporal scales. Following a necessarily brief observational overview of the solar magnetic field and its cycle, this review on solar dynamo theory is structured around three areas in which significant advances have been made in recent years: (*a*) global magnetohydrodynamical simulations of convection and magnetic cycles, (*b*) the turbulent electromotive force and the dynamo saturation problem, and (*c*) flux transport dynamos, and their application to model cycle fluctuations and grand minima and to carry out cycle prediction.
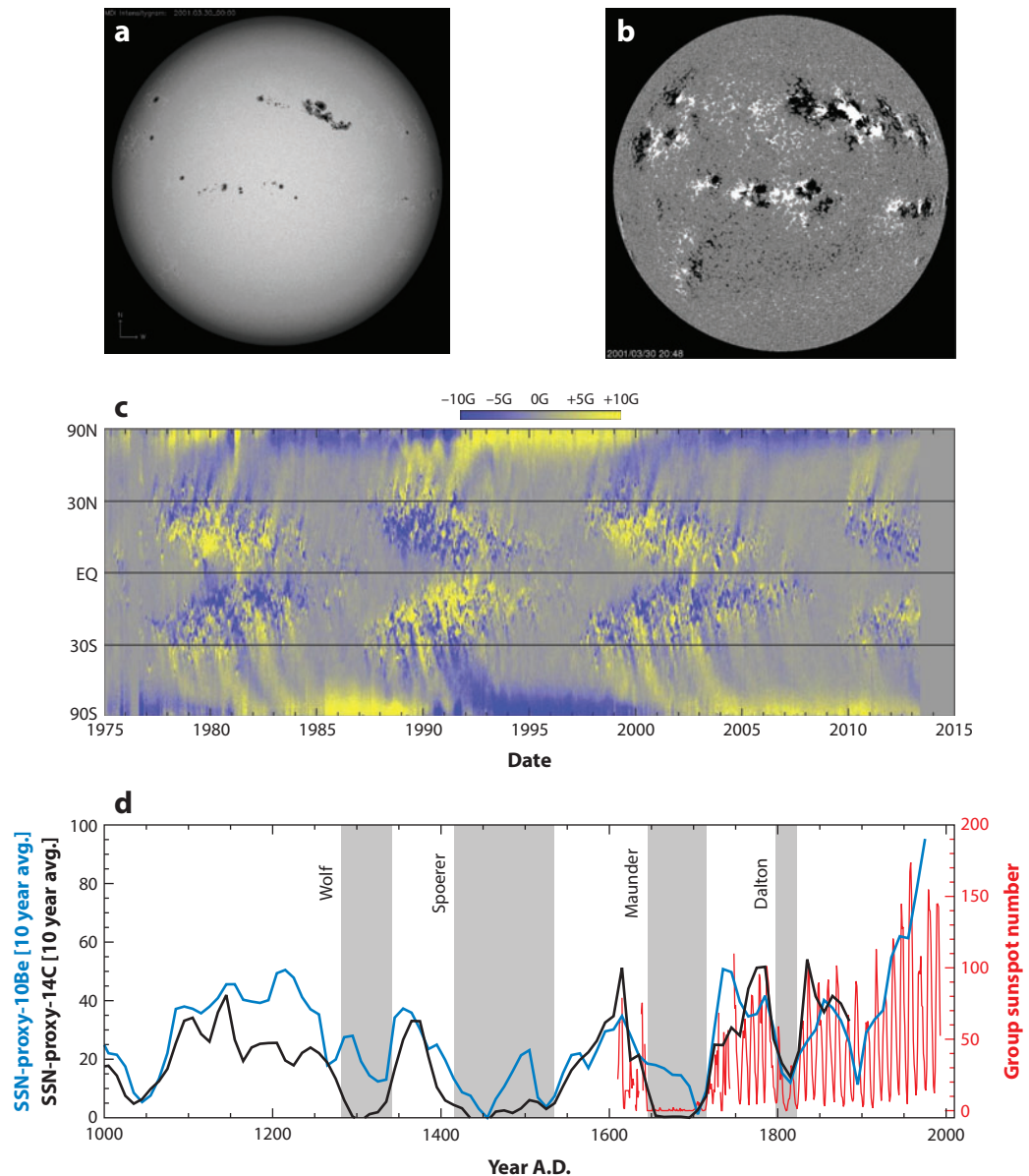
1. SOLAR MAGNETISM

Forget your old astronomy textbook; the Sun is a variable star, its variability is strongly imprinted across interplanetary space, there is no such thing as the solar constant, and the Sun's magnetic field is behind it all. It structures the solar atmosphere from the photosphere across the corona and into the solar wind and heliosphere, modulates the Sun's corpuscular and radiative output, and drives all geoeffective solar eruptive phenomena collectively defining solar activity. Nor is the Sun anomalous in this respect; every solar-type star observed with sufficient sensitivity shows similar signs of magnetically driven activity.

Numerous good reviews are available on the observational side of solar magnetism (e.g., Solanki et al. 2006, de Wijn et al. 2009); consequently, the following overview focuses on aspects most pertinent to solar dynamo theory. The solar magnetic field is structured and evolves over an astoundingly wide range of spatial and temporal scales (see **Figure 1**). Sunspots (**Figure 1*a***) are now understood to be the surface manifestations of emerging magnetic fields produced in the solar interior. Restricted to low heliocentric latitudes but seldom seen very near the equator, sunspots are the seats of strong magnetic fields ($\sim$0.1–0.5 T), and the larger sunspots usually appear in pairs of opposite magnetic polarities (*black* versus *white* on **Figure 1*b***). The favored physical picture is that of magnetic flux ropes rising from below and piercing the photosphere in the form of so-called Ω-loops (Parker 1955a, Caligari et al. 1995, Fan 2009 and references therein). The leading spots (with respect to the direction of solar rotation, from left to right in **Figure 1*a,b***) show the same magnetic polarity in each hemisphere, with this leading polarity reversing across hemispheres. These striking hemispheric regularities, known as Hale's Polarity law (Hale et al. 1919), reflect the presence of an internal magnetic field that is spatially well organized on the scale of the Sun as a whole and is antisymmetric about the solar equator.

Temporally extended observations (**Figure 1*c,d***) also reveal some remarkable large-scale order. The number of sunspots on the solar disk waxes and wanes on a timescale of about 11 years, with sunspot emergences occurring at midlatitudes in the beginning of this cycle and progressively closer to the equator as the cycle proceeds. The reversal of the relative magnetic polarities of sunspot pairs from one cycle to the next indicates that the underlying magnetic cycle has a period of twice that of the sunspot cycle. A well-defined dipole moment is also present, with the average polar cap magnetic field reaching a few 10^{-3} T at times of sunspot minimum and reversing its polarity at times of maximum sunspot counts, i.e., it lags the deep-seated sunspot-producing magnetic field by about half a sunspot cycle.

The sunspot record extends back to the beginning of the telescopic era in the early seventeenth century and, taken as a proxy of solar magnetism, makes it possible to trace the solar magnetic cycle over that time span (*red curve* on **Figure 1*d***; see also Hathaway 2010). The sunspot cycle shows significant variability in both its amplitude and duration, including an extended "quiet" epoch spanning the years 1645 to 1715, now known as the Maunder Minimum, during which very few sunspots were observed (Eddy 1976). Other indirect proxies, notably cosmogenic radioisotopes (e.g., Beer 2000, Usoskin 2013), make it possible to go much further back in time, although with some loss of temporal resolution. These data nonetheless show that episodes similar to the Maunder Minimum have occurred intermittently in the more distant past (*gray bands* in **Figure 1*d***; see also Usoskin et al. 2007, McCracken et al. 2013).

Although the strongest magnetic fields observed at the solar surface are found in sunspots, magnetographic observations also reveal their presence away from sunspots and active regions, in the form of small magnetic elements of sizes going down to the smallest spatial scale currently resolved by solar observing instruments (de Wijn et al. 2009). These small magnetic elements collectively define the magnetic network, and have sizes distributed as a power-law (Parnell et al.

Figure 1

The solar magnetic field and its cycle. (*a*) A continuum image and (*b*) a line-of-sight magnetogram, both taken on March 30, 2001, by the MDI instrument onboard SOHO (ESA/NASA). (*c*) A synoptic magnetogram (courtesy of D. Hathaway, NASA/MSFC), constructed by zonally averaging full-disk magnetograms over successive solar rotations and stacking such averages into a time-latitude diagram. (*d*) The time series of the group sunspot number (SSN; in *red*; Hoyt & Schatten 1998) together with pseudoSSN time series constructed from two cosmogenic radioisotopes (data courtesy of I. Usoskin, Sodankylä Obs.). These provide measures of the overall activity levels at lower temporal resolution but over a much longer timespan than the sunspot record.

2009) spanning at least five orders of magnitude in size, which is indicative of scale invariance. Their lifetimes are much smaller than sunspots and associated magnetic structures, as they continuously emerge, submerge, merge or cancel with other elements of same/opposite magnetic polarity (Schrijver et al. 1997). These surface processes may actually account for the observed scale invariance (Thibault et al. 2012 and references therein). The magnetic network shows little, if any, dependence on the phase of the magnetic cycle and contributes little to the net (signed) hemispheric flux. It does, however, play an important role in driving the nonthermal photospheric radiative output, especially at wavelengths shorter than the visible.

The challenge facing dynamo theory is thus to explain the existence and observed evolution of the solar magnetic field. This is an immense topic, which has already been the subject of numerous monographs (e.g., Moffatt 1978, Parker 1979, Krause & Rädler 1980, Rüdiger & Hollerbach 2004, Charbonneau 2013). The present review focuses on a few areas where significant advances have been made in the past two decades in a manner such as to complement, rather than duplicate, other recent reviews on the topic, notably Ossendrijver (2003), Brandenburg & Subramanian (2005), Miesch & Toomre (2009), and Charbonneau (2010). General aspects of magnetohydrodynamics most pertinent to magnetic field amplification in electrically conducting fluid are first briefly reviewed in Section 2. This is followed in Section 3 by a survey of recent global magnetohydrodynamical simulations of solar convection having achieved the production of large-scale magnetic fields undergoing polarity reversals. Section 4 introduces mean-field electrodynamics, both as a tool to analyze and interpret numerical simulations as well as a means of building simplified evolutionary models of the solar magnetic cycle. Section 5 focuses on a class of mean-field-like simplified dynamo models, the so-called flux transport dynamos, which have received considerable attention in recent years as they provide an attractive framework within which to understand the origin of fluctuations in solar cycle amplitude and duration and perhaps even reliably predict these characteristics for future cycles. The review closes in Section 6 with a survey of promising future research directions and outstanding challenges in solar dynamo theory.

2. FUNDAMENTALS OF MAGNETOHYDRODYNAMICS

Physical conditions in the solar interior up to the photosphere are such that the interaction of fluid flow and magnetic field is well-described by the magnetohydrodynamical approximation (hereafter MHD; see, e.g., Davidson 2001). In its classical formulation, MHD describes the behavior of an electrically neutral mixture of electrically charged microscopic constituents in which the collision frequency largely exceeds any relevant plasma frequencies. In such a (moving) collisionally dominated plasma, Ohm's law holds in a reference frame comoving with the fluid at the macroscopic scale. For a nonrelativistic fluid flow $\mathbf{u}$, the rest frame electric field $\mathbf{E}$ is then simply

$$\mathbf{E} = \mathbf{J}/\sigma - \mathbf{u} \times \mathbf{B}, \tag{1}$$

where $\mathbf{J}$ and $\mathbf{B}$ are, respectively, the current density and magnetic field, and σ is the electrical conductivity (SI units are used throughout). Excluding externally imposed rapid variations of $\mathbf{E}$ (e.g., turning batteries on or off), Ampère's law holds in its pre-Maxwellian form,

$$\nabla \times \mathbf{B} = \mu_0 \mathbf{J}, \tag{2}$$

where μ_0 is the magnetic permeability. Using this expression to substitute for $\mathbf{J}$ in Equation 1 and inserting the resulting expression for $\mathbf{E}$ into Faraday's law leads to the MHD induction equation,

$$\frac{\partial \mathbf{B}}{\partial t} = \nabla \times (\mathbf{u} \times \mathbf{B} - \eta \nabla \times \mathbf{B}), \tag{3}$$

where $\eta = (\mu_0\sigma)^{-1}$ is the magnetic diffusivity. The first term on the right-hand side expresses induction by the flow of electrically charged constituents across the magnetic field and the second Ohmic dissipation of the current systems supporting that same magnetic field, as per Equation 2. The relative importance of induction versus dissipation is measured by the magnetic Reynolds number,

$$\mathrm{Rm} = \frac{u_0 L}{\eta}, \tag{4}$$

where u_0 and L are characteristic values for the flow speed and length scale, respectively, the latter assumed here to adequately characterize the spatial variations of both the flow and magnetic field. For most astrophysically relevant circumstances, and all aspects of dynamo action considered in what follows, one finds $\mathrm{Rm} \gg 1$ if L is set equal to the scale of the system (e.g., the solar radius, $R_\odot$), indicating that Ohmic dissipation is very inefficient on this global scale.

In the infinite conductivity ideal MHD case ($\eta = 0$), Equation 3 becomes identical to the evolution equation for a line element advected by a flow $\mathbf{u}$, implying that the magnetic field lines move with the fluid (see, e.g., Davidson 2001, his section 2.7.4), a result known as Alfvén's theorem and dubbed flux freezing. The consequent ability of the fluid flow to displace, bend, and stretch magnetic field lines is crucial to all dynamo mechanisms considered in all that follows.

Dimensional analysis of Equation 3 yields two natural timescales for magnetic field evolution: the advective timescale $\tau_u = L/u_0$ and diffusive timescale $\tau_\eta = L^2/\eta$. Using again $L \sim R_\odot$ and $\eta \sim 1$ m^2 s^{-1} for the bulk of the convection zone, one obtains $\tau_\eta \simeq 10^{10}$ year, twice the age of the Sun. From this point of view, the very existence of the solar magnetic field is not an issue; any fossil magnetic field remaining from the Sun's gravitational collapse from a (weakly magnetized) molecular cloud would still be present in the solar interior at a strength hardly differing from its zero-age main-sequence value. It also implies that we must look to the flow $\mathbf{u}$ to explain the much shorter evolutionary timescales observed, from the decadal cycle period, down to minutes for the evolution of small photospheric magnetic flux concentrations. The lower end of this range is actually commensurate with the advective time of surface convection, for which $L \sim 10^6$ m and $u_0 \sim 10^3$ m s^{-1}, yielding $\tau_u \sim 15$ min. The oddity lies therefore with the large-scale magnetic field and its decadal polarity reversals. Moreover, this problem with the disparity of timescales carries over to length scales. A turbulent flow can generate strong magnetic fields on its own small spatial scale provided Rm is large enough (see, e.g., Cattaneo 1999, Cattaneo et al. 2003, Stein & Nordlund 2006, Vögler & Schüssler 2007). However, it is also quite apt at enhancing the dissipation of magnetic fields having larger spatial scales. How, then, can turbulent convection, with typical scales on the order of 10^5–10^7 m and 10^3–10^5 s, induce and sustain against dissipation a spatiotemporally coherent magnetic component with scales on the order of 10^9 m and 10^8 s? This quandary is often referred to as the magnetic self-organization problem (Tobias et al. 2011).

From the MHD induction (Equation 3) one can obtain an evolution equation for the magnetic energy (E_B) integrated over the volume V of the system (here the Sun):

$$\frac{\partial E_B}{\partial t} = -\oint_{\partial V} \mathbf{S} \cdot \hat{\mathbf{n}} \, dA - \frac{1}{\sigma} \int_V \mathbf{J}^2 \, dV - \int_V (\mathbf{u} \cdot \mathbf{F}) \, dV, \tag{5}$$

where $\mathbf{S} = \mu_0^{-1} \mathbf{E} \times \mathbf{B}$ is the Poynting flux at the domain boundary ∂V, and $\mathbf{F} = \mathbf{J} \times \mathbf{B}$ is the Lorentz (magnetic) force per unit volume acting on the plasma. The first term on the right-hand side thus measures the flux of electromagnetic energy in or out of the domain; for a star-like system embedded in vacuum, this is typically set to zero. The second term reflects the action of Ohmic dissipation, inexorably turning magnetic energy into heat. The third term is where the action is; it corresponds to the work done by the flow against the magnetic force. This is the channel through
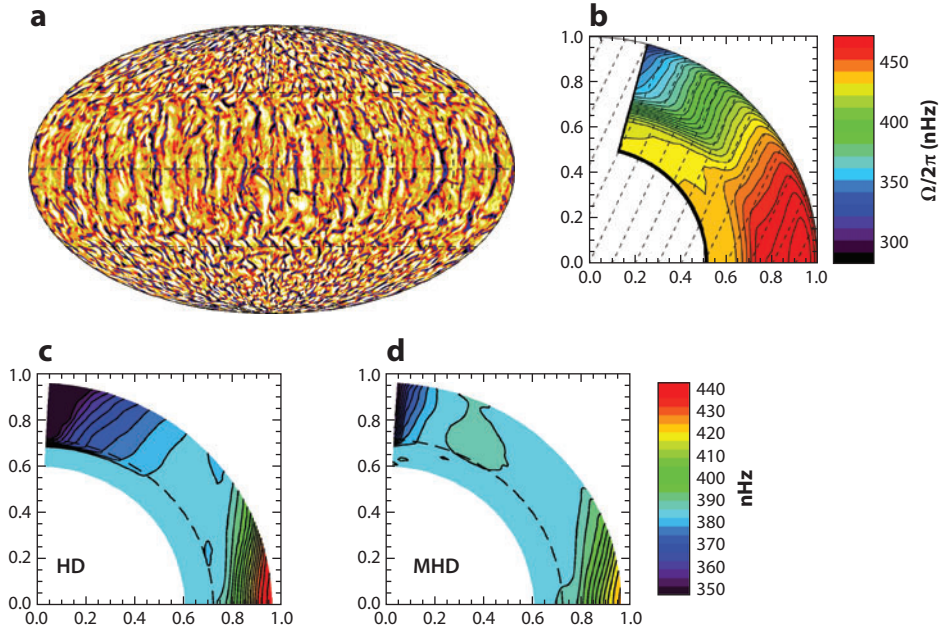
Plasma flows in the solar interior: (*a*) vertical flow velocities in subsurface layers, as produced by a high-resolution EULAG simulation, courtesy of Guerrero et al. (2013); (*b*) helioseismic inversion of the solar internal differential rotation, taken from Howe (2009); and differential rotation in (*c*) a purely hydrodynamical (HD) EULAG numerical simulation and (*d*) a EULAG numerical simulation obtained in the magnetohydrodynamic (MHD) regime. The dashed line indicates the base of the convection zone.

which the kinetic energy of the flow can be converted to electromagnetic energy, a process that must take place in a manner sufficiently efficient to offset losses due to Ohmic dissipation. This requirement is the very essence of any dynamo process.

In its simplest form, the dynamo problem consists of finding a flow **u** that, when inserted into Equation 3, leads to amplification of **B**. In principle, we are off to a good start, because vigorous flows abound in the Sun (see **Figure 2**). In the outer 30% of the Sun's radius, the luminosity is transported by thermally driven turbulent fluid motions known as convection. Inhomogeneous due to stratification, and lacking reflection symmetry due to the influence of rotation, convection at small spatial scales drives large-scale flows, notably differential rotation. These two flow components, energetically, are the primary contributors to **u** in Equations 3 and 5. Yet the magnetic force acting on the charged constituents of the fluid also resist the flow, potentially quenching it and, in doing so, turning off induction. The dynamo problem is inherently nonlinear, and therein lie the physical, mathematical, and computational challenges.

3. GLOBAL MAGNETOHYDRODYNAMICAL SIMULATIONS OF SOLAR CONVECTION

Global (i.e., full-sphere) numerical simulation of the MHD induction (Equation 3), together with the usual fluid equations augmented by the Lorentz force, is an obvious brute force way to tackle the solar dynamo problem. In practice, this is an extremely challenging task, in view of the aforementioned wide separation of spatial and temporal scale characterizing solar convection and

magnetic field evolution. However, unlike some of the simpler modeling approaches considered in Sections 4 and 5 below, such simulations do properly incorporate the magnetic backreaction on the inductive flow at all resolved spatial and temporal scales.

The underlying physics is not at all exotic, as the full set of MHD equations simply expresses conservation of mass, momentum, energy, and magnetic induction as expressed by Equation 3; the latter is duplicated here for completeness:

$$\frac{\partial \rho}{\partial t} + \nabla \cdot (\rho \mathbf{u}) = 0, \tag{6}$$

$$\frac{\partial \mathbf{u}}{\partial t} + (\mathbf{u} \cdot \nabla)\mathbf{u} = -\frac{1}{\rho}\nabla p - 2\boldsymbol{\Omega} \times \mathbf{u} + \mathbf{g} + \frac{1}{\mu_0 \rho}(\nabla \times \mathbf{B}) \times \mathbf{B} + \frac{1}{\rho}\nabla \cdot \boldsymbol{\tau}, \tag{7}$$

$$\frac{\partial e}{\partial t} + (\gamma - 1)e \, \nabla \cdot \mathbf{u} = \frac{1}{\rho}\left\{\nabla \cdot [(\chi + \chi_r)\nabla T] + \phi_u + \phi_B\right\}, \tag{8}$$

$$\frac{\partial \mathbf{B}}{\partial t} = \nabla \times (\mathbf{u} \times \mathbf{B} - \eta \nabla \times \mathbf{B}). \tag{9}$$

Here ρ is the fluid density; e is internal energy; p is gas pressure; $\boldsymbol{\tau}$ is the viscous stress tensor; χ and χ_r are the kinetic and radiative thermal conductivities, respectively; ϕ_u and ϕ_B are the viscous and Ohmic dissipation functions, respectively; and other symbols have their usual meaning. In the solar dynamo context it is customary to write the MHD equation in a rotating reference frame; the centrifugal force is absorbed in the gravitational term so that only the Coriolis force appears on the right-hand side of Equation 7. Equations 6–9 need to be augmented by an equation of state (typically the perfect gas law), and the magnetic field needs to be subjected to the solenoidal constraint $\nabla \cdot \mathbf{B} = 0$. The specification of appropriate boundary conditions completes the mathematical specification of the problem.

The anelastic approximation, in common usage in the present context, consists of introducing a time-invariant background density profile, thus replacing Equation 6 by $\nabla \cdot (\rho \mathbf{u}) = 0$, and only retaining density variations about this reference profile induced by thermal dilation; in this way sound waves are filtered out of the system, allowing larger time steps, but the crucial buoyancy force is retained.

Equations 6–9 represent a set of strongly nonlinear partial differential equations that are to be solved in a thick rotating stratified shell of electrically conducting fluid subjected to thermal forcing driving convection. The first such simulations carried out by Gilman (1983) and Glatzmaier (1984, 1985) used strongly enhanced dissipative coefficients to maintain numerical stability, but nonetheless exhibited many encouraging features, including a rapidly rotating equatorial region, the buildup of large-scale magnetic fields (but showing strong hemispheric asymmetries), magnetic field migration (but poleward rather than equatorward), and polarity reversals (although quite irregular). As ever more powerful computing platforms became available in later years, simulations could be carried out at higher resolution and using lower diffusivities, thus reaching more strongly turbulent regimes (see, e.g., Brun et al. 2004). These simulations proved to be potent dynamos, in the sense that strong magnetic fields could be generated on the spatial scale of convection, but without generating any significant large-scale magnetic component. The presence of a convectively stable, mechanically forced underlying fluid layer proved efficient at producing an axisymmetric large-scale component (Browning et al. 2006), which, however, remained resolutely steady over the time span of these simulations. By contrast, the simulations of Brown et al. (2010) achieved the buildup of large-scale magnetic fields concentrated within the low-latitudes portions of the convecting layers, but again without reversals of magnetic polarity.

Achieving solar-like cyclic polarity reversals of a large-scale magnetic component in such simulations is a very recent, exciting development, on which the remainder of this section is focused. Before reviewing the design and characteristics of these simulations, a brief detour is first required through the dynamics of rotating, stratified convection and its associated large-scale flows.

3.1. Convection and Large-Scale Flows

The dynamics of solar/stellar convection is discussed in depth in the recent review articles by Miesch (2005) and Miesch & Toomre (2009), and by Howe (2009) on the observational (helioseismic) front. The key dynamical factors are rotation and stratification, which break the homogeneity and reflection symmetry of the turbulent fluid motions, leading to latitudinal temperature differences and Reynolds stresses that power large-scale flows. The key dimensionless parameter measuring the influence of rotation is the Rossby number (Ro), defined as the ratio of inertial to Coriolis forces on the right-hand side of Equation 7, or equivalently, of the rotation period P_{rot} to the convective turnover (coherence) time τ_c:

$$\mathrm{Ro} \equiv \frac{u'_{rms}}{2\Omega \ell} \equiv \frac{P_{rot}}{\tau_c}, \tag{10}$$

where u'_{rms} and ℓ are the typical velocity and length scale of the convective eddies, respectively. With Ro ~ 0.1 in the deep convection zone, from the point of view of turbulent convection the Sun is actually a fast rotator. This leads to characteristic convective patterns, with equatorial regions organized in a longitudinal stack of latitudinally elongated banana cells, extending across equatorial latitudes up to $\pm 35°$ in the Sun, at least according to global hydrodynamical simulations (see **Figure 2**; also Busse 2002).

Rotational influences also lead to a differential rotation pattern characterized by equatorial regions rotating some 30% faster than the poles, with the underlying radiative core rotating at an intermediate rate corresponding to surface midlatitudes. This is relatively well-reproduced by numerical simulations, except for rotational isocontours being too cylindrical at low to midlatitudes, and the radial shear at low latitudes too concentrated within the convection zone, as compared with helioseismic measurements (cf. **Figure 2b,d**). In the Sun, this deviation from cylindrical isocontours is now understood to be caused by a latitudinal entropy gradient present throughout the convection zone, which results in a thermal wind balance that breaks the Taylor-Proudman theorem (Kitchatinov & Rudiger 1995, Miesch et al. 2006, Balbus et al. 2009). This has been reproduced in purely hydrodynamical numerical simulations including a stably stratified fluid layer underlying the convecting layers, as in **Figure 2c** (see also Brun et al. 2011). A thin radial shear layer is also present beneath the photosphere, and another, known as the tachocline, straddles the base of the convection zone and ensures a smooth match between the latitudinal differential rotation of the convection zone and the rigid rotation of the outer radiative core.

Meridional circulation refers to the large-scale axisymmetric flow component confined to meridional planes. It is weaker and shows more temporal variability than differential rotation. Directed poleward with speeds of ~ 10 m s^{-1} at the surface low to midlatitudes, it is also ultimately powered by convection. Observational attempts to detect the expected equatorward return flow, carried out through helioseismology or the tracking of deeply anchored magnetic tracers, have yielded conflicting results, some inferring a return flow located deep in the convective envelope, whereas others infer a shallow return flow (cf. Braun & Fan 1998, Schou & Bogart 1998, Hathaway 2012, Zhao et al. 2013). Theory (Kitchatinov & Rüdiger 1995) and numerical simulations (Miesch & Toomre 2009, see their section 3.5) indicate that multiple flow cells stacked in radius and/or latitude are indeed likely. Both differential rotation and meridional circulation show

low-amplitude cyclic variability phase locked to the magnetic cycle (see Howe 2009, see her section 9; Ulrich 2010).

3.2. Cycles and Polarity Reversals: A Survey

It is instructive to compare the flows and magnetic fields produced by three independent global simulations all working on, in principle, the same calculation: thermally driven MHD convection and dynamo action in a thick, stratified, thermally forced rotating shell of electrically conducting fluid. The virtue of this comparison lies with the fact that each of these simulations uses distinct physical approximations, treatment of subgrid dissipation, and computational methodologies. This allows, to some extent at least, identification of which patterns and behaviors are physically robust and which are not.

The PENCIL code (**www.nordita.org/pencil-code**) is a parallel high-order finite difference code operating as a direct numerical simulation (DNS), using fixed values for dissipative coefficients such as viscosity and thermal and magnetic diffusivity. The pseudoglobal compressible simulations in a spherical wedge discussed below are taken from Käpylä et al. (2010, 2012, 2013). The ASH (anelastic spherical harmonics; Clune et al. 1999) code is a massively parallel spectral code formulated in spherical geometry. It uses a large-eddy simulation (LES) approach, whereby stability is maintained through the use of an explicit subgrid model (see the sidebar, Subgrid Models). The simulation chosen here is taken from Brown et al. (2011) and makes use of a static eddy diffusivities formulation, as in earlier ASH MHD simulations (e.g., Brun et al. 2004, Browning et al. 2006, Brown et al. 2010). EULAG-MHD (Smolarkiewicz & Charbonneau 2013) is an MHD version of the EULAG code (EUlerian-LAGrangian, **www.mmm.ucar.edu/eulag/**; see also Prusa et al. 2008), a robust, parallel multiscale flow solver formulated in generalized curvilinear coordinates. It can operate an implicit large-eddy simulation (ILES; see Grinstein et al. 2007), in which dissipation is delegated to the numerical advection scheme, rather than being formulated explicitly. The simulations discussed below are of this type and are essentially identical to those discussed by Ghizaru et al. (2010) and Racine et al. (2011).

All three simulations generate convective patterns and large-scale flows that turn out remarkably similar. As expected, convection is organized in cells of hot, ascending fluid delineated by a network of narrow downflow lanes, as in purely hydrodynamical simulations. In equatorial

Animation CLICK TO VIEW

a

b

c $\langle B_\phi \rangle$, $r/R = 0.718$

d $\langle B_\phi \rangle$, $\theta = -50°$

Time (years)
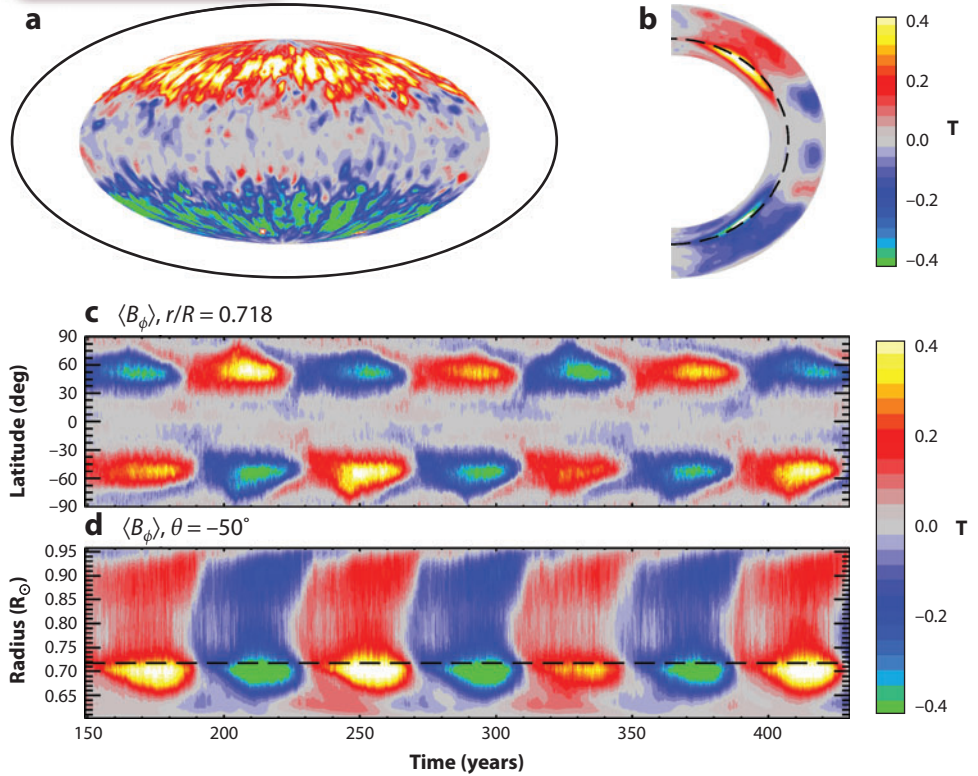
Video 1

Magnetic cycles in a global EULAG-MHD anelastic simulation, essentially identical to those by Ghizaru et al. (2010) and Racine et al. (2011). To view the video, access this article on the Annual Reviews website at **http://www.annualreviews.org**. This simulation includes a convectively stable fluid layer underlying the convecting layers. (*a*) A snapshot in Mollweide projection of the toroidal (zonal) magnetic component at depth $r/R_\odot = 0.718$; (*b*) a snapshot of the zonally averaged toroidal field in a meridional plane taken at the same time as panel *a*. (*c*) Time-latitude and (*d*) radius-latitude diagrams of the zonally averaged toroidal field, the former at depth $r/R_\odot = 0.718$ and the latter at latitude $+25°$. The dashed lines in panels *b* and *d* indicate the bottom of the convectively unstable layers. This is a moderate-resolution simulation, rotating at the solar rate but subluminous with respect to the Sun.

regions, convection again organizes itself in a longitudinal stack of elongated rolls with their axes parallel to the rotation axis (see **Figure 2***a*) (cf. Käpylä et al. 2010, their figure 2; Brown et al. 2011, their figure 3a,b; Ghizaru et al. 2010, their figure 1; and Miesch & Toomre 2009, their section 2.2.3). The mean differential rotation in all cases is characterized by equatorial acceleration with angular velocity isocontours approximately aligned with the rotational axis, but now it is a pole-to-equator angular velocity difference markedly smaller than solar (cf. Käpylä et al. 2010, their figure 1; Brown et al. 2011, their figure 3c; and Racine et al. 2011, their figure 4). Again in all three cases the mean (axisymmetric) meridional circulation is weak and highly time variable, and it shows little spatial structuring on large scales. With the axisymmetric mean subtracted, the zonally averaged flow kinetic helicity is also quite similar in all three simulations, being negative (positive) in the Northern (Southern) Hemisphere, peaking at high latitude with a secondary maximum at
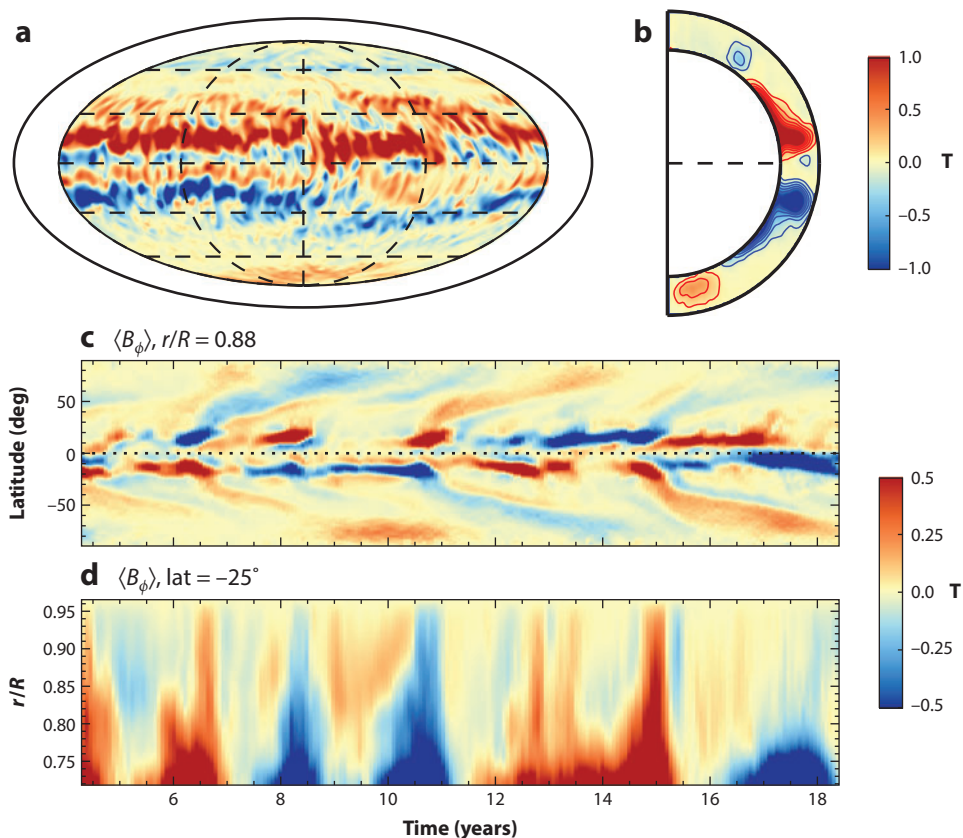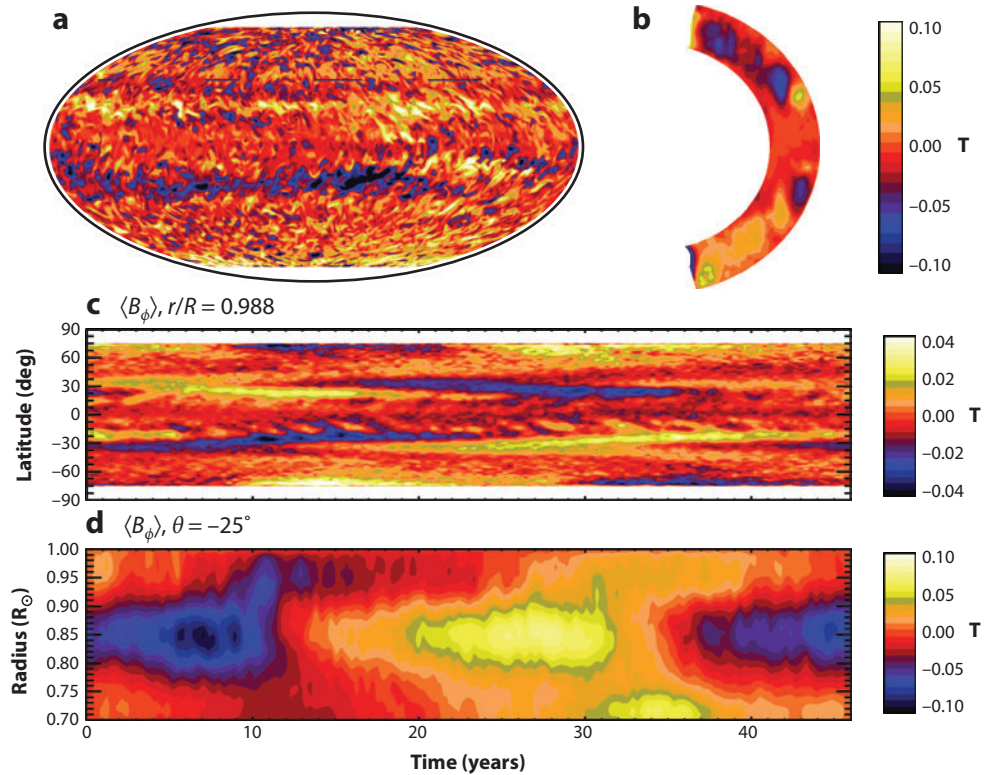
Figure 3

Identical in format to **Video 1**, but showing magnetic cycles in a global anelastic spherical harmonics simulation, specifically simulation D5 by Brown et al. (2011). This high-resolution anelastic simulation is close to the solar luminosity, rotates at five times the solar rate, and does not include a convectively stable fluid layer beneath the convecting layers. Figure provided by M. Miesch (HAO/NCAR).

low latitudes, and changing sign at the base of the convecting fluid layer (cf. Käpylä et al. 2012, their figure 2; Brown et al. 2010, their figure 8a; and Racine et al. 2011, their figure 15C).

With the flows so similar at small and large scales, one might expect that dynamo action will show comparable levels of similarity. Interestingly, this expectation is only partly borne out. **Video 1** and **Figures 3** and **4** offer different representations of the spatiotemporal evolution of a toroidal magnetic field in the three simulations considered. **Video 1** and **Figures 3a** and **4a** show snapshots in Mollweide projection of the toroidal magnetic field component at mid-depth in the convecting layers, panels *b* a zonal average in the meridional plane, and panels *c* and *d* time-latitude and radius-latitude cuts of that same zonally averaged toroidal magnetic component.

In all three simulations the magnetic field is highly turbulent, but also shows prominent banded structures fairly well aligned in the zonal direction and reaching strengths in the 0.1–1 T range. These axisymmetric toroidal field bands undergo polarity reversals that can be more or less regular and synchronized across hemispheres, depending on the specific simulation considered. All three simulations show significant accumulation of magnetic field at the base of the convecting layers, as expected of turbulent convection in a stratified environment (e.g., Tobias et al. 2001). In the

Figure 4

Identical in format to **Video 1** and **Figure 3**, but showing magnetic cycles in a PENCIL compressible simulation (case E4 in Käpylä et al. 2013). This is a high-resolution simulation in a spherical wedge excluding latitudes higher than $\pm 15°$. This simulation rotates at 4.4 times the solar rate, is superluminous as compared with the Sun, and does not include a convectively stable fluid layer beneath the convecting layers. Produced from numerical data provided by P. Käpylä (Univ. Helsinki).

EULAG-MHD simulation, the magnetic field actually peaks in the outer reaches of the stably stratified fluid layer underlying the convection zone, whereas in the ASH and PENCIL simulations strong magnetic field concentrations also build up at low latitudes within the convecting layers. The ASH and PENCIL simulations show poleward propagation at mid- to high latitudes, and the latter also exhibits solar-like equatorward propagation at low latitudes (**Figure 4c**). The axisymmetric toroidal field in the EULAG-MHD simulation of **Video 1**, by contrast, peaks at midlatitudes and only shows a hint of equatorward propagation at its high-latitude edge. The PENCIL and EULAG-MHD simulations also show upward propagation in the outer half of the convecting layers, a feature absent in the ASH simulation. The magnetic cycle periods also differ significantly: 3–6 years in ASH, ~35 years in PENCIL, and up to $\simeq 80$ years in EULAG-MHD.

All three simulations also generate cyclic modulations of large-scale flows (see Brown et al. 2010, 2011; Passos et al. 2012). Beaudoin et al. (2013) carried out a detailed analysis of the EULAG-MHD simulation of **Video 1**, where the amplitude and phase of the torsional oscillations are found to be remarkably close to those detected in the Sun via helioseismology (cf. Howe 2009, her figures 5 and 25). They could also show that torsional oscillations developing in their simulation do not simply result from the action of the Lorentz force associated with the

cyclic large-scale magnetic component, but involve magnetically mediated alteration of all other contributions to the angular momentum flux: small-scale Reynolds and Maxwell stresses, and advection of angular momentum by meridional flows.

3.3. Self-Organization of Large-Scale Magnetic Fields

All three simulations considered above are strongly turbulent, yet clearly achieve varying levels of self-organization of magnetic components characterized by spatial and temporal scales much larger/longer than those of convection. How exactly this self-organization takes place is still not understood, but various contributing factors have already been identified:

1. **Rotation**. Rotation is a powerful large-scale organizing mechanism via the action of the associated Coriolis force on convective turbulence. The Coriolis force can impart hemispheric cyclonicity on turbulence, generate latitudinal temperature gradients, and even structure convection on large scales, as in **Figure 2**. In the Sun, photospheric convection operates on timescales much shorter than the rotation period (i.e., the Rossby number Ro $\gg$ 1) and so is expected to be unaffected by rotation, whereas in the bulk of the convection zone one expects Ro $\leq$ 1, implying significant rotational influence. Indeed, otherwise identical global MHD simulations computed at varying rotation rates can exhibit very different types of magnetic self-organization; operating close to the solar luminosity, when run with the rotation lowered to three times solar, the ASH simulation of **Figure 3** develops low-latitude toroidal field bands that remain steady in time; with rotation further lowered to the solar rate, no significant large-scale field is generated. By contrast, a cousin of the EULAG-MHD simulation of **Video 1** running at close to solar luminosity requires the rotation rate to be increased to three times solar to recover reasonably regular cycles. These converging bits of empirical evidence all point to the Rossby number as a key parameter.

2. **Differential rotation**. Differential rotation powered by turbulent Reynolds stresses is a potentially powerful mechanism for spatial organization, as this flow is structured on global scales and, at least in the Sun, remains close to stationary on cycle timescales. Differential rotation is also efficient at dissipating nonaxisymmetric large-scale magnetic fields, thus also favoring the buildup of solar-like axisymmetric large-scale magnetic fields.

3. **Subgrid models**. The choice of a subgrid model to maintain nonlinear stability of the numerical solutions can have a strong impact on global characteristics of the large-scale dynamo solutions, either directly on magnetic field generation or indirectly via changes it may produce in large-scale flow contributing to magnetic field induction. For example, recent ASH simulations computed using different types of subgrid models, though otherwise identical or closely similar, achieve markedly distinct types of magnetic self-organization (cf. Brown et al. 2010, 2011; Nelson et al. 2013; K. Augustson, M.S. Miesch, & J. Toomre, manuscript in preparation).

4. **The magnetic Prandtl number**. This is the (dimensionless) ratio of viscosity to magnetic diffusivity Pm $= \nu/\eta$ and thus measures the ratio of length scales at which the flow and magnetic field transit from turbulent to laminar and dissipate. In the parameter regime Pm $>$ 1, there exist a range of length scales in which the destructive folding of the magnetic field by the flow ceases while Ohmic dissipation is still small, which should favor dynamo action. Empirical evidence from MHD numerical simulations running in the Pm $>$ 1 range indicates that this is indeed the case and that the numerical value of Pm has a significant impact on magnetic self-organization. Note, however, that Pm $<$ 1 in the bulk of the solar convection zone.

5. **The tachocline**. Stably stratified and home to significant shear that is both radial and latitudinal (e.g., **Figure 2b**), the tachocline is the ideal environment to amplify and store

the strong magnetic field that later will buoyantly rise through the convection zone and form sunspots upon emergence at the photosphere. Moreover, a wide variety of flow-field dynamical interactions can develop therein. Some may contribute to the self-organization of the large-scale magnetic field, and perhaps feed back, directly or indirectly, onto dynamo processes operating in the bulk of the overlying convection zone.

Mechanisms of self-organization notwithstanding, the simulations discussed in the preceding section are all dynamically consistent at all resolved spatial and temporal scales and therefore represent outstanding virtual laboratories allowing investigation of many key questions in solar dynamo theory. The remainder of this section focuses on three such questions, in which breakthroughs have been made in recent years.

3.4. Instabilities and Waves in the Tachocline

Large-scale magnetic fields imbedded in stably stratified stellar interiors are known to be sensitive to an astoundingly wide range of instabilities (see, e.g., Pitts & Tayler 1985, Spruit 1999, Braithwaite & Nordlund 2006). The tachocline is clearly a potential candidate, as it combines significant rotational shear, a strong magnetic field, weakly subadiabatic stratification, and possibly coupling to a fossil magnetic field in the deeper radiative interior (see Strugarek et al. 2011 and references therein). Perhaps most pertinent in this context is the class of magnetoshear instabilities investigated by Gilman & Fox (1997; see also Cally et al. 2003, Dikpati et al. 2003, and Miesch et al. 2007 and references therein). This joint MHD instability is inherently two-dimensional and nonaxisymmetric and operates in stably stratified environments, developing on spherical shells in the joint presence of a latitudinal angular velocity shear and a strong toroidal magnetic field. The instability has been found to operate for a wide range of toroidal field profiles, including latitudinally broad profiles similar to those produced in the stable fluid layers in the EULAG-MHD simulation of **Video 1**.

Miesch (2007) has presented thin-shell MHD numerical simulations demonstrating that in the presence of steady mechanical forcing of differential rotation and forced replenishment of a latitudinal magnetic field component, cyclic waxing and waning of this instability can take place; the toroidal field and differential rotation are first destroyed by the growth of the instability, then rebuilt through the forcing terms following nonlinear saturation. This leads to a characteristic pattern where the magnetic energies associated with the axisymmetric background toroidal field and nonaxisymmetric components resulting from the growth of the instability both oscillate with a well-defined period, the latter lagging the former by $\sim\pi/2$ in phase (see Miesch 2007, his figure 2). **Figure 5** shows equivalent time series for axisymmetric (*black*) and nonaxisymmetric (*blue*) magnetic field energies in the stable layers of the EULAG-MHD simulation of **Video 1**. The periodic behavior and $\sim\pi/2$ phase offset are both clearly apparent, even though here the mechanical and magnetic forcing occurs "naturally" through the action of turbulent Reynolds stresses and the operation of the dynamo in the overlying convecting layers. Ongoing analyses of this simulation (N. Lawson & P. Charbonneau, submitted) indicates that the preferred mode of instability has an azimuthal wavenumber $m = 3$ or sometimes $m = 4$, unlike in the simulation analyzed by Miesch (2007), where the $m = 1$ "clamshell" mode dominates, in agreement with linear theory (see Gilman et al. 2007).

The striking similarities between **Figure 5** and Miesch's (2007) figure 2 do not strictly prove that the same physical instability is at play in both cases, but nonetheless they strongly suggest that some kind of related magnetoshear instability operates in the stably stratified deep layers of the simulation. This raises a number of interesting questions: Is this instability the primary mechanism saturating the amplitude of the deep-seated dynamo-generated large-scale magnetic
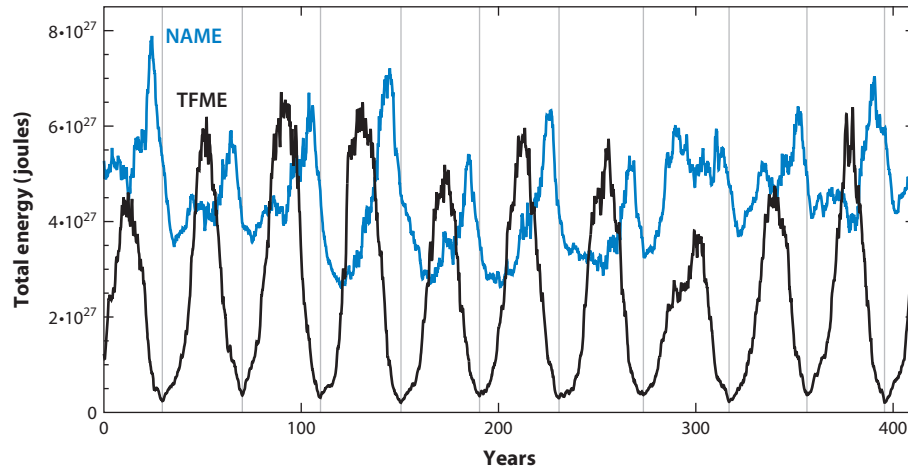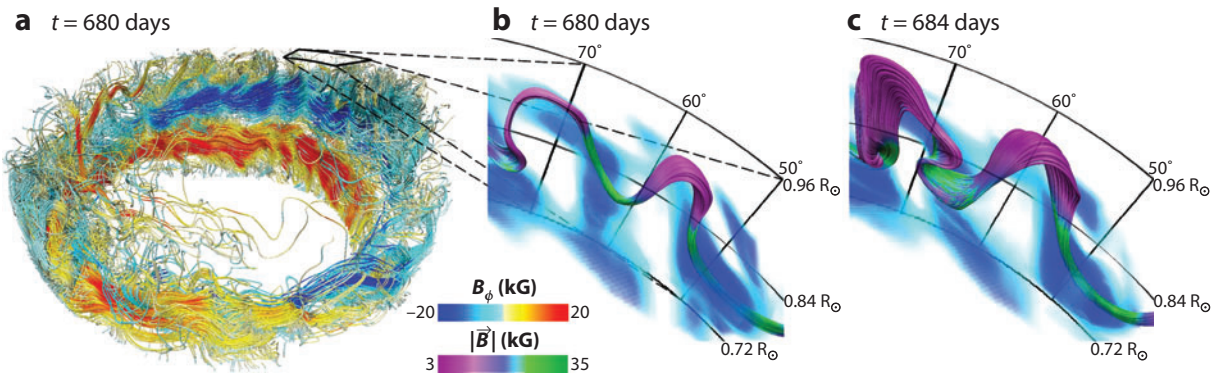
Figure 5

Magnetic energy evolution in the tachocline in the EULAG-MHD simulation of **Video 1**. The magnetic energy associated with the zonally averaged (axisymmetric) toroidal magnetic field is plotted in black and labeled TFME (toroidal field magnetic energy), and that comprising all other nonaxisymmetric contributions is plotted in blue, labeled NAME (nonaxisymmetric magnetic energy). Here the magnetic energies are volume-integrated in the Southern Hemisphere over the depth range $0.602 \leq r/R \leq 0.693$, which excludes the strongly turbulent, thin convective overshoot layer developing immediately beneath the base of the convecting layers ($r/R = 0.718$ in this simulation). Both energies oscillate with a well-defined period identical to that of the magnetic cycle and maintain a well-defined phase lag of about $\pi/2$ for most cycles. Compare with Miesch (2007, his figure 2).

field? Is it a mere by-product of a dynamo operating autonomously in the convecting layers or does it feed back into the dynamo process? Is the timescale for the growth and decay of the instability entirely set by the dynamo period imposed from above or is the growth of the instability playing a role in the global polarity reversals? Moreover, and to be discussed further below in Section 4.6, the development of some of these instabilities can drive an electromotive force, which could then power a dynamo contained entirely within the tachocline.

Another potentially important aspect of tachocline dynamics involves the excitation of internal gravity waves by convective overshoot as well as the contribution such waves might make on the dynamics of the tachocline and radiative core (e.g., Talon et al. 2002, Kim & MacGregor 2003, Rogers & Glatzmaier 2006, Rogers et al. 2008, Brun et al. 2011) and, indirectly, on dynamo action via their impact on the rotational shear. Already difficult to model in the purely hydrodynamical regime because of the extreme disparity of spatial and temporal scales between the waves and the large-scale flows, gravity wave dynamics is further complicated by the presence of magnetic fields. Geometrically simplified models (Barnes et al. 1998) and numerical simulations (Rogers & MacGregor 2011) both indicate that gravity wave propagation, absorption, and attendant angular momentum transport are all strongly altered by the presence of strong magnetic fields within the tachocline.

3.5. Coherent Structures and Sunspot Formation

A recent exciting development in global MHD numerical simulations of solar convection is the spontaneous production of strongly magnetized flux strands in the ASH simulations by Nelson et al. (2011, 2013). This process is favored by the strong turbulent intermittency characterizing these simulations, which make use of a dynamical subgrid-scale model for dissipation, as opposed

a $t = 680$ days **b** $t = 680$ days **c** $t = 684$ days

B_ϕ (kG)
−20 ▮▮▮ 20

$|\vec{B}|$ (kG)
3 ▮▮▮ 35

Figure 6

Formation and rise of rope-like magnetic flux systems in the toroidal wreaths produced by the ASH simulations by Nelson et al. (2013). The superequipartition-strength magnetic flux strands form as substructures within the toroidal wreaths and expand as they rise through the convecting layers. Reproduced from Nelson et al. (2013, their figure 18) with permission.

to the static eddy-diffusivity formulation characterizing most earlier ASH simulations (e.g., **Figure 3**). **Figure 6** shows an example, taken from Nelson et al. (2013, their figure 18). Many of these flux strands, forming within existing low-latitude toroidal wreaths, are pulled away by strong convective updraft but have developed enough of a density deficit in their cores for magnetic buoyancy to contribute to their rise through the convecting layers.

Further analyses of many such buoyant loop events by Nelson et al. (2014) have shown that most manage to maintain their approximately east-west orientation as they rise through the turbulent environment of the modeled convection zone, and therefore upon emergence would comply with Hale's Polarity law. This reopens the possibility that the sunspot-forming magnetic fields could be generated and stored entirely within the convection zone, challenging the currently prevalent view that the magnetic flux ropes giving rise to sunspots are stored, and perhaps even formed, in the overshoot layer beneath the base of the convection zone.

3.6. Magnetic Modulation of Convective Energy Transport

Another recent exciting development is the detection of a magnetically mediated modulation of convective energy transport in a set of EULAG-MHD simulations, including that shown in **Video 1** (Cossette et al. 2013). In the anelastic approximation the convective luminosity (enthalpy) crossing a spherical surface takes the form

$$L_c = \iint \rho c_p u_r \tilde{T} \, dS, \tag{11}$$

where $\tilde{T}$ is the temperature fluctuation about the mean value on the shell. One might rightfully expect that the Lorentz force will resist the convective flow, thus reducing u_r, and therefore that the convective energy flux should be smaller at the peak of magnetic cycles than at times of polarity reversals. In fact, precisely the opposite behavior is observed in the simulation; energy transport varies in phase with the magnetic cycle, as shown in **Figure 7**. This in-phase positive correlation ($r = +0.63$ over the 1,300-year span of this simulation) can be traced to an enhancement of the stronger convective plumes, accompanied by a reduction of negative convective flux contributions by turbulent entrainment, i.e., cold fluid pushed upward, warm fluid pushed downward. Interestingly, the probability density function of vertical turbulent velocities remains essentially invariant across the cycles, indicating that the magnetic field is somehow altering the correlation
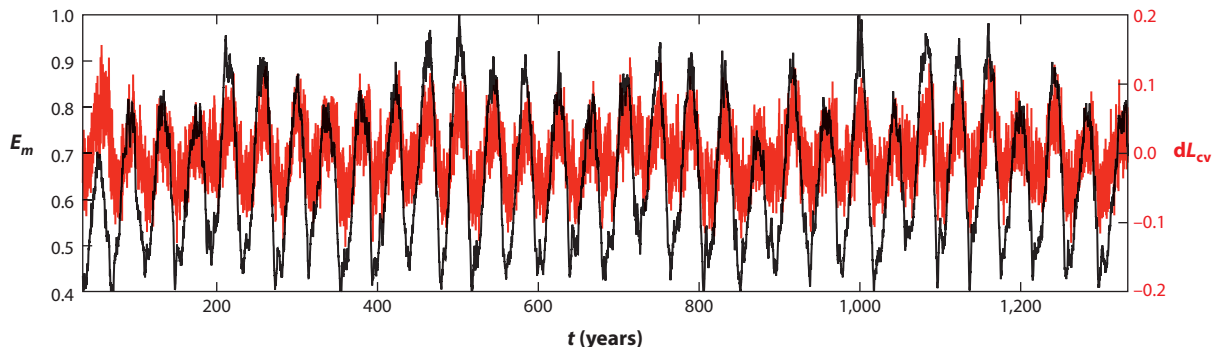
Figure 7

Time series of total magnetic energy (*black*) and convective luminosity (*red*) in the EULAG-MHD simulation of **Video 1**. The two time series vary in phase, with a linear correlation coefficient $r = +0.63$. Temporally extended version of Cossette et al. (2013, their figure 4).

between vertical velocities and temperature perturbations. How exactly this takes place is still being investigated, but the important point is that a variation of the total irradiance in phase with the magnetic cycle is also observed on the Sun (see, e.g., Fröhlich & Lean 2004 and references therein). The simulation from which the time series of **Figure 7** is extracted is actually subluminous as compared with the Sun, yet here the peak-to-peak convective luminosity variation, if scaled to the solar luminosity, amounts to $\sim$0.3%, which compares favorably with the observed decadal variation in total solar irradiance.

Although the varying coverage of magnetic structures clearly dominates irradiance variations on timescales going from minutes to weeks, the possibility that part (or even all) of the variations over timescales decadal and up could be owing to internal structural/convective changes has been a topic of great debate for over three decades now (e.g., Li & Sofia 2001, Foukal et al. 2006, Fröhlich 2009). Global MHD simulations have reached the point where the underlying physical mechanism can perhaps be pinned down, and a "smoking gun" observational signature identified.

4. MEAN-FIELD ELECTRODYNAMICS

The same wide disparity of spatial and temporal scales making direct numerical simulations so challenging can also be capitalized upon via a mathematical approach known as mean-field electrodynamics in order to design much simpler dynamo models capturing only the "slow" spatiotemporal evolution of the large-scale magnetic component. For nearly half a century, mean-field electrodynamics has served as the workhorse of solar dynamo modeling, and is consequently very well-covered in a number of recent and not-so-recent monographs and review articles (Moffatt 1978, Parker 1979, Krause & Rädler 1980, Hoyng 2003, Ossendrijver 2003, Rempel 2006a). After an overview of its theoretical underpinnings and associated mathematical formulation, the following focuses primarily on recent developments, including the use of the mean-field approach as an interpretive framework to investigate the nature of dynamo action observed in numerical simulations.

4.1. The Turbulent Electromotive Force

At the core of mean-field electrodynamics is the hypothesis of scale separation between the small-scale flow and field (here convection and the turbulent magnetic field it generates) and the large-scale flow and field (here differential rotation, meridional circulation, and the magnetic component

associated with the solar cycle). The total flow and field are thus each separated into these two components:

$$\mathbf{B} = \langle \mathbf{B} \rangle + \mathbf{b}', \quad \mathbf{U} = \langle \mathbf{U} \rangle + \mathbf{u}', \tag{12}$$

where the angular brackets denote averaging over an intermediate length scale, sufficiently larger than the scales characterizing $\mathbf{u}'$ and $\mathbf{b}'$ so that $\langle \mathbf{u}' \rangle = 0$ and $\langle \mathbf{b}' \rangle = 0$. This is not a linearization, as no assumptions are being made regarding the magnitude of $\mathbf{u}'$ versus $\langle \mathbf{U} \rangle$, or $\mathbf{b}'$ versus $\langle \mathbf{B} \rangle$. Inserting Equation 12 into the MHD induction (Equation 3) and applying this generic averaging operator leads to the mean-field induction equation:

$$\frac{\partial \langle \mathbf{B} \rangle}{\partial t} = \nabla \times (\langle \mathbf{U} \rangle \times \langle \mathbf{B} \rangle + \boldsymbol{\xi} - \eta \nabla \times \langle \mathbf{B} \rangle), \tag{13}$$

where $\boldsymbol{\xi} = \langle \mathbf{u}' \times \mathbf{b}' \rangle$ is the mean electromotive force (hereafter emf) produced by correlated fluctuations of the flow and field at small scales. As we shall see presently, the key point is that this emf can act as a source term for $\langle \mathbf{B} \rangle$. If Equation 12 is inserted into the MHD induction equation, without averaging but now subtracting Equation 13, one obtains an evolutionary equation for the small-scale field:

$$\frac{\partial \mathbf{b}'}{\partial t} = \nabla \times (\langle \mathbf{U} \rangle \times \mathbf{b}' + \mathbf{u}' \times \langle \mathbf{B} \rangle + \mathbf{u}' \times \mathbf{b}' - \boldsymbol{\xi} - \eta \nabla \times \mathbf{b}'). \tag{14}$$

Now, the whole point of the mean-field approach is not to have to deal explicitly with small scales, so formally solving Equations 13 and 14 as a coupled system is out of the question. Observe, however, that if $\mathbf{u}'$ is considered to be given, Equation 14 is linear in $\mathbf{b}'$, with a source term $(\mathbf{u}' \times \langle \mathbf{B} \rangle)$ linear in $\langle \mathbf{B} \rangle$; similarly, with $\langle \mathbf{U} \rangle$ and $\mathbf{u}'$ given, Equation 13 is linear in $\langle \mathbf{B} \rangle$, with $\boldsymbol{\xi}$ providing a source term linear in $\mathbf{b}'$. It follows that the mean emf can be expressed as a linear (tensorial) development in terms of the large-scale magnetic field:

$$\mathcal{E}_i = \alpha_{ij} \langle B \rangle_j + \beta_{ijk} \frac{\partial \langle B \rangle_j}{\partial x_k} + \cdots, \tag{15}$$

where the tensors α_{ij}, β_{ijk}, etc., depend on the properties of the flow, but cannot depend on $\langle \mathbf{B} \rangle$. With closure achieved in this manner, specifying the form of these tensors becomes the crux of the matter. For homogeneous, isotropic turbulence, $\alpha_{ij} = \alpha \delta_{ij}$ and $\beta_{ijk} = \beta \epsilon_{ijk}$; truncating Equation 15 after the second term and substituting in the mean-field induction (Equation 13) then yields

$$\frac{\partial \langle \mathbf{B} \rangle}{\partial t} = \nabla \times (\langle \mathbf{U} \rangle \times \langle \mathbf{B} \rangle + \alpha \langle \mathbf{B} \rangle - (\eta + \beta) \nabla \times \langle \mathbf{B} \rangle). \tag{16}$$

The α term now emerges as a (mean) turbulent electromotive force aligned with the mean-magnetic field, in contrast to the usual motional emf $\langle \mathbf{U} \rangle \times \langle \mathbf{B} \rangle$, which is perpendicular to $\langle \mathbf{B} \rangle$. This contribution to the total turbulent emf, crucial in many dynamo models discussed below, is known as the α-effect, and is nonzero for flows lacking reflection symmetry. The β term reduces to an additive contribution to the magnetic diffusivity η and can thus be interpreted as turbulent diffusion of $\langle \mathbf{B} \rangle$. The α- and β-effects in Equation 16 embody, respectively, constructive and destructive folding of the mean-magnetic field by the small-scale flow. There is no free lunch here; turbulence may, under certain circumstances to be elucidated presently, yield a mean-electromotive force acting as a source for the mean-magnetic field, but it also inevitably provides enhanced dissipation of that same mean-magnetic field.

Because they relate to the intrinsic topological properties of the flow, α and β are in principle computable if the small-scale flow—or at least its statistical properties—are known. Even in such a case, when all is said and done, the calculation is tractable only in a few specific physical regimes (see, e.g., Ossendrijver 2003, Rempel 2006a): The first is for turbulent flows in which

the correlation time τ_c is smaller than their turnover time ℓ/u'_{rms}, where ℓ and u'_{rms} are typical values for the turbulent eddies. The ratio of these two quantities is known as the Strouhal number $\mathrm{St} = \tau_c u'_{\mathrm{rms}}/\ell$, so the requirement is $\mathrm{St} < 1$. The second tractable regime is that of low magnetic Reynolds number turbulent flows, i.e., $\mathrm{Rm} \ll 1$. The third applies to situations in which the magnetic field is dominated by its large-scale component, i.e., $|\mathbf{b}'| \ll |\langle\mathbf{B}\rangle|$. For near-homogeneous, near-isotropic turbulence satisfying at least one of these criteria, the α and β coefficients in Equation 16 take these forms:

$$\alpha = -\frac{\tau_c}{3}\langle\mathbf{u}' \cdot \nabla \times \mathbf{u}'\rangle, \tag{17}$$

$$\beta = \frac{\tau_c}{3}\langle(\mathbf{u}')^2\rangle. \tag{18}$$

The β-effect is here proportional to the turbulent intensity. Within the convection zone, with $|\mathbf{u}'| \sim 10\ \mathrm{m\ s^{-1}}$, the magnitude of β is expected to exceed that of η by many orders of magnitude. The α-effect, by contrast, is proportional to the mean kinetic helicity. Cyclonic flows are thus prime candidates for driving an α-effect (Parker 1955b). In the solar/stellar context, this cyclonicity is imparted on horizontally expanding convective updrafts and converging downdrafts by the Coriolis force, thus creating a strong correlation between vertical flow speed and helicity.

The right-hand sides of Equations 17 and 18 have the benefit of being relatively straightforward to extract from numerical simulations. However, for solar interior conditions one expects $\mathrm{Rm} \gg 1$, $\mathrm{St} \sim 1$, and $|\mathbf{b}'|/|\langle\mathbf{B}\rangle| > 1$, which violates the conditions under which these expressions are physically valid. Nonetheless, empirical evidence discussed further below (Section 4.3) indicates that Equations 17 and 18 hold rather well at moderately high Rm, $\mathrm{St} \sim 1$, and $|\mathbf{b}'|/|\langle\mathbf{B}\rangle| \sim 1$.

Returning to the general tensorial formulation of the emf, it is possible to separate the α-tensor in symmetric and antisymmetric contributions:

$$\alpha_{ij} = \alpha_{ij}^S - \varepsilon_{ijk}\gamma_k, \tag{19}$$

so that the mean emf becomes

$$\mathcal{E}_i = \alpha_{ij}^S\langle\mathbf{B}\rangle_j + [\boldsymbol{\gamma} \times \langle\mathbf{B}\rangle]_i + \beta_{ijk}\frac{\partial\langle\mathbf{B}\rangle_j}{\partial x_k} + \cdots. \tag{20}$$

Substitution into the mean-field induction (Equation 13) reveals that $\boldsymbol{\gamma}$ emerges therein as an additive contribution to $\langle\mathbf{U}\rangle$, i.e., it acts on $\langle\mathbf{B}\rangle$ as would a large-scale flow. Under the same physical conditions under which Equations 17 and 18 can be expected to hold, it can be expressed as

$$\boldsymbol{\gamma} = -\frac{\tau_c}{3}\nabla\langle(\mathbf{u}')^2\rangle, \tag{21}$$

i.e., it is proportional to the negative gradient of turbulent intensity. This pseudoflow is known as general turbulent pumping and is increasingly recognized as a potentially important contributor to the evolution of the solar large-scale magnetic field. In particular, with u'_{rms} decreasing with increasing depth in the solar convection zone, downward pumping is expected all the way through the bottom of the convecting layers. This has indeed been observed in a variety of numerical simulations (e.g., Tobias et al. 2001, Ossendrijver et al. 2002, Ziegler & Rüdiger 2003, Racine et al. 2011). The off-diagonal elements of the symmetric part α_{ij}^S also represent turbulent pumping, but they are specific to individual field components and therefore cannot be subsumed into an advective pseudoflow (see discussion by Ossendrijver et al. 2002).

Whichever forms are assumed for the α and β-tensors, their specifications achieve closure, in the sense that with $\langle\mathbf{U}\rangle$ also specified, the mean-field induction (Equation 13) can be solved for $\langle\mathbf{B}\rangle$. This forms the basis of mean-field dynamo models, which offer a modeling approach much simpler than the numerical simulations reviewed in the preceding section. They allow, among

other things, efficient exploration of parameter space and the tackling of questions and issues related to long-timescale behavior (e.g., **Figure 1d**), otherwise inaccessible in practice to bona fide MHD numerical simulations.

4.2. Axisymmetric Mean-Field Dynamo Models

The large-scale magnetic field associated with the solar cycle being axisymmetric to a reasonable degree, the averaging operator of the mean-field approach can then be associated naturally with a zonal average. Working in spherical polar coordinates (r, θ, ϕ) and for the time being considering only differential rotation, the large-scale flow and field can be written as

$$\langle \mathbf{U} \rangle (r, \theta, t) = r \sin \theta \Omega (r, \theta, t) \hat{\mathbf{e}}_\phi, \tag{22}$$

$$\langle \mathbf{B} \rangle (r, \theta, t) = B(r, \theta, t) \hat{\mathbf{e}}_\phi + \nabla \times [A(r, \theta, t) \hat{\mathbf{e}}_\phi], \tag{23}$$

where Ω is the angular velocity of rotation, $B\hat{\mathbf{e}}_\phi$ is the toroidal magnetic field (zonally oriented), and the toroidal vector potential $A\hat{\mathbf{e}}_\phi$ defines the poloidal magnetic field (component in meridional planes). We first restrict ourselves to the kinematic approximation, in which the magnetic backreaction of $\langle \mathbf{B} \rangle$ on $\langle \mathbf{U} \rangle$ is neglected, so that Ω is considered to be given. Substituting these expressions into Equation 13 allows the separation of the mean-field induction equation into two coupled evolution equations for A and B:

$$\frac{\partial A}{\partial t} = \eta \left(\nabla^2 - \frac{1}{\varpi^2} \right) A + \alpha B, \tag{24}$$

$$\frac{\partial B}{\partial t} = \eta \left(\nabla^2 - \frac{1}{\varpi^2} \right) B + \varpi (\nabla \times A\hat{\mathbf{e}}_\phi) \cdot (\nabla \Omega) + \hat{\mathbf{e}}_\phi \cdot \nabla \times (\alpha \nabla \times A\hat{\mathbf{e}}_\phi), \tag{25}$$

with $\varpi = r \sin \theta$, and for constant η and an isotropic (diagonal) α-effect. These expressions highlight the crucial role of the α-effect. The associated turbulent emf is the sole source term appearing on the right-hand side of Equation 24, unlike in Equation 25 where shearing by differential rotation also acts as a source for B. Indeed, without the αB source term in Equation 24, Cowling's theorem ensures that an axisymmetric flow cannot sustain an axisymmetric magnetic field against Ohmic dissipation (see Moffatt 1978, his section 6.4).

Dimensional analysis allows us to measure the relative importance of the various source terms in Equations 24 and 25 through the dynamo numbers:

$$C_\alpha = \frac{\alpha_0 R_\odot}{\eta_0}, \quad C_\Omega = \frac{\Omega_0 R_\odot^2}{\eta_0}, \tag{26}$$

where α_0, Ω_0, and η_0 are characteristic measures of the magnitude of the α-effect, large-scale rotational shear, and net (turbulent) magnetic diffusivity, respectively. In the solar case, with $\alpha_0 \sim 1 \text{ m s}^{-1}$, one finds $C_\alpha \ll C_\Omega$, implying that rotational shearing of the large-scale poloidal magnetic component by differential rotation dominates the induction of the toroidal component. On this basis, the turbulent emf contribution is often omitted from Equation 25, resulting in the $\alpha\Omega$ dynamo model, whereas retaining all components of ξ yields the $\alpha^2\Omega$ dynamo model. Dynamo action is also possible in the absence of rotational shear (i.e., $C_\Omega = 0$), which results in the α^2 dynamo model.

As shown analytically by Parker (1955b) for semi-infinite Cartesian geometry, the $\alpha\Omega$ dynamo model supports traveling-wave-like solutions and offers a simple and elegant explanation for the observed equatorward migration of sunspot belts in the course of the solar cycle (e.g., **Figure 1**). This behavior is robust, in that it carries over to spherical geometry (e.g., Yoshimura 1975, Stix

1976) and to the $\alpha^2\Omega$ regime provided shear remains significant (Choudhuri 1990, Charbonneau & MacGregor 2001). In the $\alpha\Omega$ regime, dynamo waves propagate along isocontours of angular velocity Ω, in a direction $\mathbf{s}$ given by

$$\mathbf{s} = \alpha\nabla\Omega \times \hat{\mathbf{e}}_\phi. \tag{27}$$

In the solar context, equatorward propagation at low latitude arises if the $\alpha_{\phi\phi}$ tensor component is negative in the Northern Hemisphere, and the dynamo is restricted to the equatorial portion of the tachocline, where $\nabla\Omega \simeq d\Omega/dr > 0$ (see **Figure 2b**).

4.3. Measuring the α-Effect

The α-effect is a kinematic property of turbulent flows and as such can in principle be calculated under specific physical, geometrical, and statistical assumptions; for example, an important and influential early result owing to Steenbeck & Krause (1969) concerns the crucial $\alpha_{\phi\phi}$ tensor component, which can be expressed as

$$\alpha_{\phi\phi} \simeq -\frac{16}{15}\tau_c^2(u'_{\mathrm{rms}})^2\Omega \cdot \nabla\ln(\rho u'_{\mathrm{rms}}). \tag{28}$$

With u'_{rms} increasing more slowly outward than ρ is decreasing across the convection zone (according to mixing length estimates) and Ω pointing north, $\alpha_{\phi\phi}$ turns out positive (negative) in the Northern (Southern) Hemisphere. For u'_{rms} depending only on depth, Equation 28 also predicts that the magnitude of $\alpha_{\phi\phi}$ should peak at the poles and vary with polar angle as $\cos\theta$. It also predicts a sign change near the base of the convecting layers, as u'_{rms} is expected to vanish rapidly as one moves downward into the convectively stable radiative core, leading to $\nabla(\rho u'_{\mathrm{rms}}) > 0$.

Alternately, the α-effect can be directly measured in numerical simulations of turbulent convection. This is not as straightforward as one may imagine. In principle, applying a uniform large-scale field on a statistically stationary numerical simulation of turbulent convection—or any turbulent flow for that matter—allows the measurements of the emf so generated; the original flow provides the $\mathbf{u}'$, and its inductive action on the imposed large-scale field generates the $\mathbf{b}'$, from which the mean emf $\boldsymbol{\xi} = \langle\mathbf{u}' \times \mathbf{b}'\rangle$ is computed by suitable spatiotemporal averaging. The individual components of the α-tensor are then readily computed by projecting the emf on the applied mean-field. This imposed field method has been used on a variety of local and global simulations of thermally-driven convection in stratified, rotating environments (see, e.g., Brandenburg et al. 1990; Ossendrijver et al. 2001, 2002; Ziegler & Rüdiger 2003; Cattaneo & Hughes 2006). Such calculations have allowed exploration of the dependence of the α-effect on rotation rate, stratification, etc. Particularly pertinent in the solar context are simulations of thermally-driven convection in local Cartesian boxes positioned at various latitudes set by the imposed inclination of the rotation vector $\boldsymbol{\Omega}$ (see, e.g., Brummell et al. 1996), allowing easier access to more strongly turbulent regimes than would global simulations. Surprisingly, many of these numerical experiments have corroborated at least qualitatively some key predictions of mean-field theory, including Equation 28, even though the simulations are typically run in parameter regimes under which closure expressions such as Equations 17, 18, or 21 are not expected to hold. In particular, at moderately low rotation rates, in the sense that the inverse Rossby number $\mathrm{Ro}^{-1} \equiv \Omega\tau_c < 1$, the critical (from the point of view of axisymmetric mean-field dynamos) $\alpha_{\phi\phi}$ component is positive (negative) in the Northern (Southern) Hemisphere, peaks in polar regions, decreases monotonically toward the equator, and exhibits a sign change near the base of the convecting layers (Ossendrijver et al. 2001), all of which is in general agreement with Equation 28. However, even a modest increase in rotation rate is found to shift the peak of the α-effect to low latitudes (Käpylä et al. 2006a). At most rotation rates explored, the α-tensor is full, in that its off-diagonal components have magnitudes comparable to their diagonal counterparts, which is indicative of the break in homogeneity caused

by stratification and rotation. As a consequence, significant turbulent pumping is also present, downward-directed in the bulk of the convecting layers but showing in addition a significant equatorward latitudinal component at mid- to low latitudes, in the meter-per-second range for the toroidal component (Ossendrijver et al. 2002). Such calculations have also shown that the components of the α-tensor are strongly fluctuating quantities, with standard deviations about the mean comparable to the magnitude of the mean (see, e.g., Ossendrijver et al. 2001, their figure 3).

To reliably measure the α-effect of the original turbulent flow in this manner, it is essential for the applied magnetic field not to alter the flow and for the flow itself not to act as a small-scale dynamo autonomously producing its own $\mathbf{b}'$ independently of the applied large-scale field. The second of these constraints can be satisfied by restricting the analysis to magnetic Reynolds numbers smaller than those at which small-scale dynamo action is sustained. Working with very weak imposed fields can bypass the first constraint, provided the averaging is carried out on time segments over which the induced $\mathbf{b}'$ also remains sufficiently weak. Producing a time series long enough to yield stable averages may then require periodic resetting of the field to low values or the combination of statistically independent shorter simulation segments. The test-field method (Schrinner et al. 2007; see also Käpylä et al. 2009) aims at bypassing both constraints simultaneously by solving a set of evolution equations for $\mathbf{b}'$, which is essentially Equation 14 herein but with a set of imposed weak test fields replacing $\langle \mathbf{B} \rangle$ on the right-hand side with the small-scale flow $\mathbf{u}'$ taken directly from the simulation being analyzed. Even then, the results turn out to be sensitive to what one would normally have hoped to be "details," such as the size and aspect ratio of the simulation box, boundary conditions, and convective parameter regime [see the discussion by Hughes & Cattaneo (2008) and Hughes et al. (2011)].

A somewhat distinct situation arises in MHD numerical simulations that autonomously produce a large-scale magnetic field in their statistically stationary saturated state; in such cases, one can choose an averaging operator, directly measure $\langle \mathbf{B} \rangle$ (rather than impose it), define $\mathbf{u}' \equiv \mathbf{u} - \langle \mathbf{U} \rangle$ and $\mathbf{b}' \equiv \mathbf{B} - \langle \mathbf{B} \rangle$, compute $\boldsymbol{\xi} = \langle \mathbf{u}' \times \mathbf{b}' \rangle$, and then reconstruct the individual components of the α-tensor. The tensor measured in this manner is no longer a kinematic property of the flow per se, but rather a measure of the net turbulent induction in the nonlinearly saturated dynamo simulation (on this point see also Hubbard et al. 2009).

Assuming a scalar α-effect (i.e., $\boldsymbol{\xi} = \alpha \langle \mathbf{B} \rangle$), Brown et al. (2010, 2011) failed to find a satisfactory relationship between the turbulent emf and the large-scale magnetic field measured in their simulations. Working with a EULAG-MHD simulation essentially identical to that shown in **Video 1**, Racine et al. (2011) introduced a method for calculating the components of the full α-tensor based on a least-squares fit of the tensorial relation:

$$\xi_i(t) = \alpha_{ij} \langle B \rangle_j(t), \quad i, j = r, \theta, \phi, \tag{29}$$

on the time series of $\boldsymbol{\xi}$ and $\langle \mathbf{B} \rangle$ at each grid point of the meridional plane in their simulation (the zonal direction being the averaging direction). The fit itself is carried out separately for each vector component of $\boldsymbol{\xi}$ and $\langle \mathbf{B} \rangle$ using singular value decomposition (SVD). Sample results of this procedure are shown in **Figure 8a** for the $\alpha_{\phi\phi}$ component, and the associated standard deviation of the fit is plotted in **Figure 8b**. In this specific instance, the fit spans 16 full magnetic cycles. Breaking the time series into segments and carrying out the fitting procedure on each segment confirms the temporal steadiness of the α-tensor, implying that the measured cyclicity of the emf is directly associated with the cyclicity of the mean-magnetic field.

Examination of **Figure 8** indicates that the $\alpha_{\phi\phi}$ component is positive in the Northern Hemisphere, peaks at the pole, and shows a sign change near the base of the convecting layer, in agreement with Equation 28 as well as with the Cartesian box calculations discussed above. A secondary peak at low latitudes is also present. Except in the equatorial region, where both $\boldsymbol{\xi}$ and
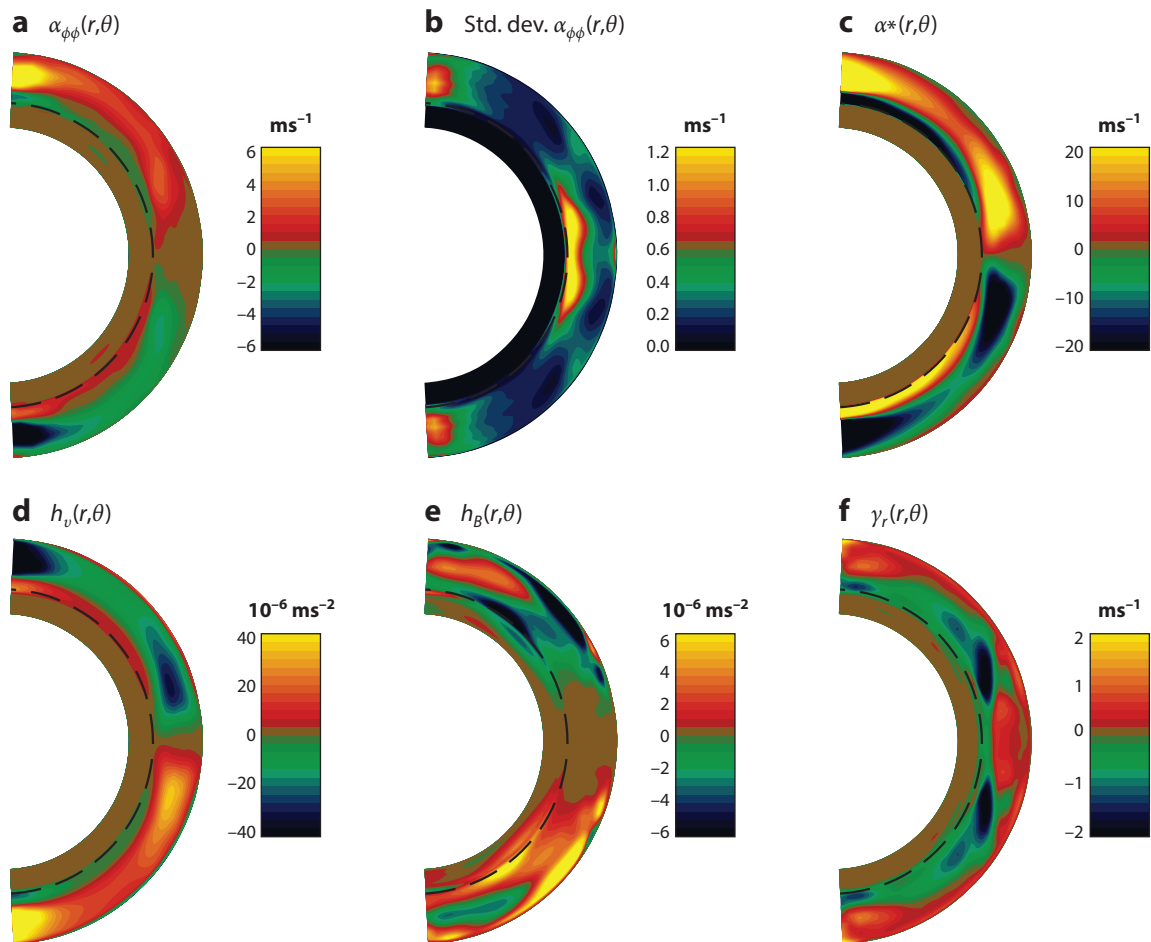
Figure 8

The α-tensor in the EULAG-MHD simulation of **Video 1**. (*a*) The $\alpha_{\phi\phi}$ component as extracted by linear least-squares fit on Equation 29, and (*b*) the associated standard deviation. (*c*) α as reconstructed via Equation 17, using the kinetic helicity profile in panel *d*, as extracted from the simulation. (*e*) The extracted current helicity profile (see Section 4.5). (*f*) The vertical turbulent pumping velocity, constructed from the full α-tensor via Equation 19.

$\langle \mathbf{B} \rangle$ are quite weak, and in the stable layer, where $\langle \mathbf{B} \rangle$ can be large but $\boldsymbol{\xi}$ is very weak, the magnitude of $\alpha_{\phi\phi}$ significantly exceeds the standard deviation returned by the SVD fit.

Figure 8c shows the α-coefficient computed via Equation 17; the kinetic helicity has been extracted from the same simulation (**Figure 8d**), and the correlation time estimated as H_ρ/u'_{rms}, where H_ρ is the density scale height. The match with the true $\alpha_{\phi\phi}$ in **Figure 8a** is remarkable, although the latter has a magnitude that is smaller by a factor of about five. Interestingly, if this mismatch is attributed to an overestimate of the correlation time τ_c, then a peculiar internal consistency is recovered; writing $\tau_c = H_\rho/u'_{\mathrm{rms}}$ amounts to setting the Strouhal number St $= 1$, but reducing it to St $= 0.2$ to match the magnitudes of **Figure 8a,c** brings us back to the regime St < 1, where Equation 17 is now expected to hold.

Figure 8f shows the radial component of the turbulent pumping velocity (e.g., Equation 19), as reconstructed from the antisymmetric component of the full α-tensor. Here again, pumping is

predominantly downward in the bulk of the convecting layers and into the upper portion of the underlying stably stratified fluid layer. The upper boundary condition causes a rapid reduction of the turbulent intensity moving up across the subsurface layers, which leads to upward turbulent pumping, in agreement with Equation 21. Except in subsurface layers, equatorward latitudinal pumping is also observed at most latitudes, peaking at 2–3 m s^{-1} at $\pm 25°$ latitude.

It is quite noteworthy that very distinct numerical simulations and equally distinct means of measuring the α-tensor in rotating, stratified thermally-driven convective turbulence simulations yield α-tensors that often show a surprising degree of agreement with each other, as well as with closed-form expressions used outside of their nominal range of validity. This is not always the case with mechanically forced helical flows (see Courvoisier et al. 2006 and references therein). The distinction hinges on the varying degrees of spatial coherence characterizing each class of flows (Courvoisier et al. 2009).

4.4. Magnetic Helicity and Its Constraint on Dynamo Action

Magnetic helicity is a topological measure of linkage between magnetic flux systems (Berger & Field 1984). In a closed system, i.e., without helicity flux through its boundaries, the total helicity evolves according to

$$\frac{\mathrm{d}}{\mathrm{d}t} \int \mathbf{A} \cdot \mathbf{B} \, \mathrm{d}V = -2\mu_0\eta \int \mathbf{J} \cdot \mathbf{B}\mathrm{d}V, \tag{30}$$

where the vector potential $\mathbf{A}$ is such that $\mathbf{B} = \nabla \times \mathbf{A}$. In the ideal limit $\eta \to 0$, which is the relevant limit for dynamo action in the interior of the Sun and stars, the right-hand side vanishes. Equation 30 then indicates that total helicity must be conserved or at best vary on the "long" diffusive timescale τ_η. This puts a strong constraint on the amplification of any magnetic field that has a net helicity, which is certainly the case with the large-scale solar magnetic field, comprised as it is of well-defined axisymmetric poloidal and toroidal components; indeed, any nontrivial axisymmetric field defined through Equation 23 is clearly helical, as the vector potential defining the poloidal component is colinear with the toroidal magnetic component. How, then, can any field amplification be achieved?

One obvious way to bypass the constraints posed by Equation 30 is to allow helicity fluxes through the outer boundary of the dynamo region, here the solar photosphere. This idea is supported by simulations (e.g., Brandenburg & Dobler 2001) as well as photospheric measurements (e.g., Kusano et al. 2002, Démoulin & Berger 2003). In particular, coronal mass ejections are suggested to be a primary contributor to the net outward helicity flux (Low 2001). Recent numerical simulations of helically-forced turbulence akin to the spherical wedge PENCIL simulations described in Section 3 and including a simplified outer "corona" do eject helicity in intermittent bursts (Warnecke et al. 2011), and this process is found to enhance dynamo action (Warnecke et al. 2012). However, it remains unclear whether the photospheric outward helicity flux makes a significant contribution to the global internal magnetic helicity budget (Berger & Ruzmaikin 2000).

It is also possible to bypass the helicity conservation constraints by having the dynamo produce helicity of opposite signs at large and small spatial scales (Brandenburg 2001). Following the scale separation logic already introduced in Section 4.1, and because $\mathbf{J}$ and $\mathbf{A}$ are linearly related to $\mathbf{B}$, the total vector potential and electric current density can be written as $\mathbf{A} = \langle\mathbf{A}\rangle + \mathbf{a}'$ and $\mathbf{J} = \langle\mathbf{J}\rangle + \mathbf{j}'$. Substituting into Equation 30 and averaging leads to an evolution equation for the helicity associated with the large-scale field:

$$\frac{\mathrm{d}}{\mathrm{d}t} \int \langle\mathbf{A}\rangle \cdot \langle\mathbf{B}\rangle\mathrm{d}V = +2 \int \boldsymbol{\xi} \cdot \langle\mathbf{B}\rangle\mathrm{d}V - 2\mu_0\eta \int \langle\mathbf{J}\rangle \cdot \langle\mathbf{B}\rangle\mathrm{d}V, \tag{31}$$

where $\boldsymbol{\xi} = \langle \mathbf{u}' \times \mathbf{b}' \rangle$ is the usual turbulent emf. Subtracting Equation 31 from the unaveraged form of Equation 30 then yields an evolution equation for the helicity of the small-scale magnetic component:

$$\frac{\mathrm{d}}{\mathrm{d}t} \int \langle \mathbf{a}' \cdot \mathbf{b}' \rangle \mathrm{d}V = -2 \int \boldsymbol{\xi} \cdot \langle \mathbf{B} \rangle \mathrm{d}V - 2\mu_0 \eta \int \langle \mathbf{j}' \cdot \mathbf{b}' \rangle \mathrm{d}V. \tag{32}$$

Observe that in the ideal limit, the total helicity—now the sum of Equations 31 and 32—is still conserved, as the first term on the right-hand side of Equations 31 and 32 are identical but for their sign. This also indicates that the turbulent emf leads to the buildup of helicity of opposite signs at large and small spatial scales, corresponding to a dual cascade away from the generation scale (Brandenburg 2001). The cascade to small scales is attractive because, in principle, Ohmic dissipation can operate efficiently there, whereas it is expected to be insignificant at larger scales. Under this view the buildup of the large-scale magnetic field is controlled by the rate at which helicity can be transported and dissipated at small scales. However, this accumulation of magnetic helicity—and magnetic energy—at small scales has profound consequences for the operation of the α-effect.

4.5. The Nonlinear α-Effect

Constructive folding of the large-scale magnetic field $\langle \mathbf{B} \rangle$, as embodied in the α-effect, requires work exerted against the magnetic tension force. If $\langle \mathbf{B} \rangle$ is amplified exponentially by dynamo action, there will inevitably come a point when the flow will no longer be able to deform the magnetic field; this turning point defines the equipartition field strength (B_{eq}), at which the magnetic energy density becomes equal to the kinetic energy density of the flow, i.e., $\mu_0^{-1} B_{\mathrm{eq}}^2 = \rho (u'_{\mathrm{rms}})^2$. Near the base of the solar convection zone, where $\rho \simeq 10^2$ kg m^{-3} and $u'_{\mathrm{rms}} \sim 10$ m s^{-1}, one has $B_{\mathrm{eq}} \sim 0.1$ T, which is comparable with sunspot field strengths. This idea forms the basis of the α-quenching formalism, which consists of introducing an explicit $\langle \mathbf{B} \rangle$-dependence to the α-tensor components via an ad hoc algebraic relation of the form

$$\alpha_{ij}(\langle \mathbf{B} \rangle) \rightarrow \frac{\alpha_{ij}}{1 + (\langle \mathbf{B} \rangle^2 / B_{\mathrm{eq}}^2)}. \tag{33}$$

From a purely practical point of view, when inserted into the mean-field dynamo equations, this expression "does the right thing," in that $\alpha_{ij} \rightarrow 0$ when $\langle \mathbf{B} \rangle$ grows beyond equipartition; it remains of common usage in mean-field dynamo modeling. The situation turns out to be nowhere near as simple, however. Working with a mechanically forced "toy" flow, Cattaneo & Hughes (1996) carried out a series of numerical experiments at varying magnetic Reynolds number Rm and found that their results did not fit Equation 33, but rather the closely related form

$$\alpha_{ij}(\langle \mathbf{B} \rangle) \rightarrow \frac{\alpha_{ij}}{1 + \mathrm{Rm}(\langle \mathbf{B} \rangle^2 / B_{\mathrm{eq}}^2)} \tag{34}$$

(see also Blackman & Brandenburg 2002). This result, which came to be known as catastrophic quenching, has profound implications for astrophysical dynamos in general, because in most astrophysically relevant situations Rm $\gg 1$, implying saturation of the large-scale field at a factor $\sqrt{\mathrm{Rm}}$ smaller than equipartition. In the solar interior, Rm $\sim 10^{10}$ leads to a saturation at the level $|\langle \mathbf{B} \rangle| \sim 10^{-6}$ T, which is now a long way from sunspot field strengths.

A pioneering measurement of the α-effect in numerical simulations by Pouquet et al. (1976) indicates that in nonlinearly saturated helical MHD turbulence, Equation 17 picks up a magnetic

contribution of sign opposite to that associated with the kinetic helicity:

$$\alpha = -\frac{\tau_c}{3}(\langle \mathbf{u}' \cdot \nabla \times \mathbf{u}' \rangle - \rho^{-1}\langle \mathbf{j}' \cdot \mathbf{b}' \rangle). \tag{35}$$

The second term on the right-hand side is the mean current helicity associated with the small-scale magnetic field and is closely related to magnetic helicity (think spectrally!). The cascade of turbulent helicity to small scales, required for the buildup of a large-scale magnetic component, thus inevitably leads to the growth of current helicity, which then quenches the α-effect. This idea has been successfully implemented in mean-field dynamo models by complementing the mean-field dynamo equation with an evolution equation for small-scale magnetic helicity driven by helicity buildup at large scales (e.g., Blackman & Brandenburg 2002, Kleeorin et al. 2003, Chatterjee et al. 2011, Hubbard & Brandenburg 2012), a procedure known as dynamical α-quenching.

Figure 8*e* shows the mean current helicity in the EULAG-MHD simulation of Video 1. Comparison with the mean kinetic helicity in Figure 8*d* reveals that both are of opposite sign over a large portion of the meridional plane, although here the kinetic helicity exceeds the current helicity by a factor of about five.

Equation 35 also allows, in principle, a sign change in the α-effect in the nonlinearly saturated regime, if the second term on the right-hand side dominates the first. Something akin to this may be at play in the simulations by Käpylä et al. (2012, 2013), where poleward propagation of the low-latitude toroidal field in the kinematic growth phase of the large-scale dynamo switches to equatorward propagation following nonlinear saturation (see Käpylä et al. 2012, their figure 3; see also Figure 4 herein), consistent with a sign change in the α-effect.

4.6. Instabilities and Dynamo Action in the Tachocline

The aforementioned difficulties encountered with conventional mean-field dynamo models, in particular catastrophic quenching of the turbulent α-effect, have motivated the study of alternate dynamo mechanisms operating in the tachocline, where amplification and storage of strong magnetic fields is in principle easier than in the strongly turbulent overlying convection zone. The class of magnetoshear instabilities discussed in Section 3.4 has been shown to generate kinetic helicity as it develops, which could, upon acting on a pre-existing large-scale toroidal magnetic field, drive an α-effect-like poloidal field regeneration mechanism (Dikpati & Gilman 2001, Dikpati et al. 2003).

Another related potential dynamo mechanism involves the development, through the action of the Coriolis force, of helical waves along the axis of a toroidal flux rope undergoing buoyant destabilization (Ferriz-Mas et al. 1994, Ossendrijver 2000b). In either case, with tachocline differential rotation shearing this poloidal field into a toroidal component sustaining the instability, a complete dynamo loop can be produced, residing entirely within the tachocline [these dynamo models are discussed further by Charbonneau (2010, his section 4)].

4.7. Recent Progress in Mean-Field Dynamo Modeling

The design of solar cycle models based on mean-field electrodynamics remains a very active field of research. Recent progress focuses on models bypassing catastrophic α-quenching by spatially separating the α-effect and the strong toroidal fields produced by rotational shearing. These interface dynamos (Parker 1993) can achieve the desired result (Charbonneau & MacGregor 1996), but tend to be rather sensitive to modeling details and so far have not satisfactorily reproduced solar cycle characteristics (see also Tobias 1996, Petrovay & Kerekes 2004).

Another very active research thrust in mean-field dynamo modeling involves the relaxation of the kinematic approximation; solving an evolution equation for the magnetically driven, time-dependent deviation ($\langle\mathbf{U}'\rangle$) from the imposed (steady) large-scale flow ($\langle\mathbf{U}\rangle$),

$$\frac{\partial\langle\mathbf{U}'\rangle}{\partial t} = \frac{\Lambda}{\mu_0\rho}(\nabla\times\langle\mathbf{B}\rangle)\times\langle\mathbf{B}\rangle + \mathrm{Pm}\nabla^2\langle\mathbf{U}'\rangle, \tag{36}$$

and the total flow is now given by

$$\mathbf{u}(\mathbf{x}, t, \mathbf{B}) = \langle\mathbf{U}\rangle(\mathbf{x}) + \langle\mathbf{U}'\rangle(\langle\mathbf{B}\rangle(\mathbf{x}, t)) \tag{37}$$

(see Tobias 1997, Moss & Brooke 2000). Solving Equation 36 together with the $\alpha\Omega$ form of Equations 24 and 25 yields a nonkinematic mean-field dynamo in which the cycle amplitude develops modulations on timescales longer than the cycle via the magnetically driven modulation of differential rotation (see, e.g., Tobias 1997, Küker et al. 1999, Brooke et al. 2002, Bushby 2006 and references therein). The period of this modulation is usually found to scale with the inverse of the magnetic Prandtl number Pm. This offers a possible explanation for Maunder Minimum-like episodes of reduced activity, if the internal field strength falls below the threshold for sunspot formation, while allowing for residual magnetic activity, as during the Maunder Minimum (Beer et al. 1998).

4.8. Mean-Field Electrodynamics as a Probe on Magnetohydrodynamic Simulations

The large-scale flows and α-tensor extracted from global numerical simulations can be reinserted into the kinematic axisymmetric mean-field dynamo (Equations 24 and 25) to ascertain the degree to which the resulting large-scale magnetic field resembles what is produced by the numerical simulations. This seemingly circular exercise can actually help pin down the mode of dynamo action operating in these simulations and disentangle aspects of magnetic field evolution associated with the nonlinear backreaction on the large-scale flow (see Käpylä et al. 2006b, Simard et al. 2013, Dubé & Charbonneau 2013).

One interesting conclusion to arise from such analyses is that even though the underlying toroidal structures are often not strictly axisymmetric, the common tendency for poleward migration observed in many global MHD simulations (e.g., **Figure 3c**; also Dubé & Charbonneau 2013, their figures 7 and 8) can be understood at some level in terms of classical dynamo waves. With the northern hemispheric $\alpha_{\phi\phi} > 0$ in the bulk of the convection zone and low-latitude differential rotation increasing outward on isocontours approximately parallel to the rotation axis (e.g., **Figure 2**), propagation away from the equatorial plane is predicted by Equation 27.

Käpylä et al. (2006b) used the α-tensor extracted from their local MHD convection simulations (Käpylä et al. 2006a) to construct $\alpha^2\Omega$ kinematic axisymmetric mean-field dynamo models that proved to exhibit a number of solar-like characteristics, including equatorward migration of the large-scale magnetic fields, although the latter was found to peak at too-high latitudes as compared with solar observations. Simard et al. (2013) carried out a similar exercise using the full α-tensor extracted from the EULAG-MHD simulation of **Video 1**, again as input into a kinematic α-quenched $\alpha^2\Omega$ model. Their mean-field dynamo solution showed many similarities with the axisymmetric magnetic component building up in the parent global MHD simulations (Simard et al. 2013, their figure 5). By selectively zeroing out various combinations of tensorial components, they could demonstrate the importance of turbulent pumping and that the complex form of the α-tensor could support cycling solutions even in the absence of differential rotation (see also Rüdiger et al. 2003).

The Simard et al. (2013) $\alpha^2\Omega$ solution also reproduced the observed tendency of the global simulation to produce "double cycles," i.e., spatially segregated dynamo modes with distinct cycle periods. This tendency can be understood upon noting that differential rotation is typically strongest at the equator and decreases toward the poles (e.g., **Figure 2**), whereas most α-tensor components, including $\alpha_{\phi\phi}$, peak at the pole and decrease in magnitude toward the equator (see **Figure 8a**). Interestingly, hints of such double cycle behaviors have been detected for many years in indicators of solar activity (e.g., Mursula et al. 2003) and more recently in acoustic oscillation frequencies, suggesting a subphotospheric origin (Fletcher et al. 2010). The numerical experiments of Simard et al. (2013) thus support the notion that there may be two large-scale dynamos operating in the Sun (see also Benevolenskaya 1995, 1998; Mason et al. 2002; Brandenburg 2005).

The mean-field machinery can also offer some useful hints as to the manner in which magnetic self-organization takes place in the global simulations. Consider the mean-field induction equation in the limit where dissipation is inefficient at large spatial scales:

$$\frac{\partial \langle \mathbf{B} \rangle}{\partial t} = \nabla \times (\langle \mathbf{U} \rangle \times \langle \mathbf{B} \rangle + \boldsymbol{\xi}). \tag{38}$$

Now, the turbulent emf $\boldsymbol{\xi} = \langle \mathbf{u}' \times \mathbf{b}' \rangle$ can be expected to vary on the "short" advective timescale associated with $\mathbf{u}'$, which is much smaller than the cycle period of $\langle \mathbf{B} \rangle$. The large-scale flow $\langle \mathbf{U} \rangle$, if it varies significantly, will also vary on this "long" cycle timescale. The only way for $\langle \mathbf{B} \rangle$ to remain quasi-steady on the convective timescale is to have

$$\langle \mathbf{U} \rangle \times \langle \mathbf{B} \rangle + \boldsymbol{\xi} \equiv \boldsymbol{\varepsilon} \simeq 0; \tag{39}$$

the small residual emf $\boldsymbol{\varepsilon}$ (small in the sense that $|\boldsymbol{\varepsilon}| \ll |\langle \mathbf{U} \rangle \times \langle \mathbf{B} \rangle|$ and $|\boldsymbol{\varepsilon}| \ll |\boldsymbol{\xi}|$) drives the evolution of $\langle \mathbf{B} \rangle$ on the long timescale. That the small- and large-scale emfs should conspire to nearly cancel each other out in this manner is rather counterintuitive, but has actually been observed in global numerical simulations producing either steady or cycling large-scale magnetic fields (Brown et al. 2010, Racine et al. 2011). This offers a possible explanation as to why magnetic self-organization on large scales seems to be such a sensitive affair. Varying numerical treatment of small-scale dissipation through explicit or implicit subgrid models will surely affect the turbulent emf to some extent; even if the differences introduced by the choice of subgrid model were small (and available empirical evidence indicates that they are not) a small relative change in $\boldsymbol{\xi}$ can still translate into a large change in the residual $\boldsymbol{\varepsilon}$, perhaps even changing its sign. Computational "details" matter!

5. FLUX TRANSPORT DYNAMOS

With the turbulent α-effect positive (negative) in the bulk of the convection zone's Northern (Southern) Hemisphere, coupled to the primarily latitudinal rotation therein, low-latitude equatorward propagation of dynamo waves is problematic unless dynamo action is concentrated in the equatorial portion of the tachocline, where $d\Omega/dr > 0$, and the α-effect experiences a sign change. Unfortunately, the two instabilities discussed in Section 4.6 both yield a positive α-effect in the Northern Hemisphere, which is not surprising because in all cases it is the Coriolis force that sets the sign of the kinetic helicity. One appealing strategy to bypass this problem is to invoke a large-scale meridional flow, directed equatorward at the base of the convection zone, to bodily advect the magnetic field and thus achieve dynamo-wave-like equatorward propagation of the sunspot-forming toroidal magnetic component in the course of the cycle (e.g., Choudhuri et al. 1995, Durney 1995, Küker et al. 2001, Pipin & Kosovichev 2011). These solar cycle models are generically known as flux transport dynamos.

One specific class of such models, the so-called Babcock-Leighton dynamos, has received increasing attention in recent years because of their ability to reproduce many observed cycle fluctuation patterns, including Maunder-Minimum-like intermittent episodes of suppressed activity, and they have even been used to predict characteristics of upcoming solar cycles. Partially eclipsed for a time by the rise of mean-field electrodynamics, they offer a very attractive alternative to turbulent dynamos based on the α-effect, and the bulk of this section is consequently dedicated to these models.

## 5.1. Surface Flux Evolution and the Babcock-Leighton Mechanism

Large sunspots often appear in pairs of opposite magnetic polarity; the member of the pair that is farther ahead in the direction of solar rotation lies closer to the solar equator than the trailing member. A line segment connecting both members thus shows a tilt with respect to the east-west direction, and this tilt increases with increasing latitude, a pattern known as Joy's law (Hale et al. 1919). Because leading/following polarities of sunspot pairs are opposite in both solar hemispheres, in their decay phase the leading member tends to experience more cross-equatorial diffusive cancellation with the leading member of sunspot pairs located in the other hemisphere, leading to the accumulation, in each hemisphere, of magnetic flux having the polarity of the trailing member. Transport of this magnetic flux to the pole by meridional circulation and/or diffusion then leads to the reversal of the polar cap field from the previous activity cycle and subsequent buildup of a net dipole moment of polarity opposite to that present in the rising phase of the cycle (Babcock 1961; and **Figure 9**). This process shows up clearly in synoptic solar magnetograms (e.g., **Figure 1c**).

This surface magnetic flux evolution is readily computable by solving the MHD induction equation on a spherical shell subjected to the advective and shearing action of surface differential rotation, poleward meridional flow, diffusion, and injection of tilted bipolar sunspot pairs (Wang et al. 1989, Wang & Sheeley 1991, Baumann et al. 2004, Jiang et al. 2013). One example is shown in **Figure 9b**. The similarity with the observed synoptic magnetogram shown in **Figure 1c** is quite remarkable. Such simulations reveal that the bulk of the magnetic flux contained in bipolar sunspot pairs experiences resistive decay and that only a small fraction makes it to the solar poles. With a mean polar field strength of $\sim 10^{-3}$ T, the polar cap magnetic flux is $\sim 10^{14}$ Wb; this is similar to the total unsigned flux in a single large bipolar sunspot pair and three orders of magnitude lower than the total unsigned magnetic flux emerging in active regions in the course of a typical activity cycle. The conversion efficiency required of the Babcock-Leighton mechanism is therefore quite modest.

The east-west tilt of sunspot pairs is crucial to the operation of the Babcock-Leighton mechanism and originates from the action of the Coriolis force on the flow developing along the axis of a sunspot-forming magnetic flux rope during its rise through the convection zone (Fan et al. 1993, D'Silva & Choudhuri 1993, Caligari et al. 1995). The pattern of tilt compatible with Joy's law turns out to be only possible in a finite range of magnetic intensity; flux ropes with field strengths inferior to about 1 T are deflected to high latitude and emerge with randomized tilts even if they survive their rise through the turbulent convection zone. Beyond ~ 10 T, by contrast, the tilt vanishes because the ropes rise to the photosphere too rapidly for the Coriolis force to have time to act. This implies that there exist both lower and upper thresholds on the internal toroidal magnetic field for the Babcock-Leighton mechanism to operate.

5.2. Magnetic Flux Transport: Meridional Flow, Diffusion, and Turbulent Pumping

Because sunspot pairs represent the surface manifestation of a deep-seated toroidal magnetic component, globally the Babcock-Leighton mechanism produces a (surface) poloidal magnetic
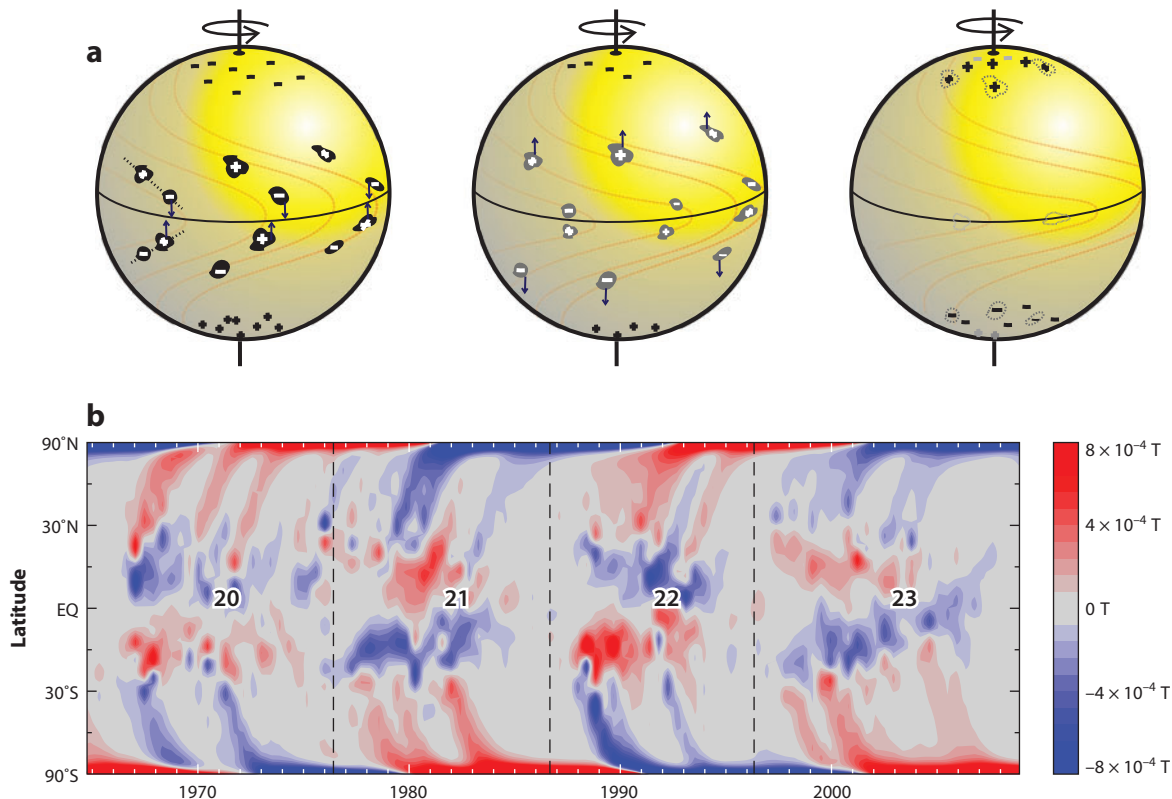
Figure 9

The Babcock-Leighton mechanism, illustrated (*a*) in diagrams and (*b*) via a 2D surface magnetic flux transport simulation covering the years 1965–2009 (activity cycles 20 to 23, numbered from one activity minimum to the next, as delineated by *vertical dashed lines*). On this latter plot, showing the variation with latitude and time of the zonally averaged surface radial magnetic field component (measured in teslas), transport to the poles shows up as inclined streaks extending poleward from low latitudes, where active region emergence takes place. Note how polarity reversal of the polar cap magnetic field occurs at about the time of activity maximum, 4–5 years after cycle onset. Compare panel *b* with the synoptic magnetogram plotted on **Figure 1c**. Graphics in panel *a* produced by D. Passos (CENTRA/IST), simulation in panel *b* by A. Lemerle (Univ. Montréal).

component from a (deep) toroidal component. Because the trailing polarity is identical to that of the original underlying toroidal field and is that which accumulates at the pole, the polarity of the dipole moment produced is identical to that of the deep-seated toroidal field. This is conceptually similar to the action of a positive α-effect in mean-field electrodynamics. In conjunction with the shearing of this poloidal field by differential rotation, a complete dynamo loop can thus be constructed, without invoking the turbulent α-effect as a source term on the right-hand side of Equation 24. However, here the poloidal and toroidal source terms are spatially segregated, with the Babcock-Leighton mechanism operating in the surface layers, whereas toroidal field amplification and magnetic flux rope formation and storage are presumably taking place at or immediately beneath the base of the convection zone. These two source regions need to be coupled to close the dynamo loop. The first Babcock-Leighton solar cycle models (Babcock 1961, Leighton 1969) assumed the sunspot-generating toroidal magnetic field to reside in the subphotospheric layers, so this coupling issue was not deemed problematic. With the formation and storage site of magnetic flux ropes now pushed down to the tachocline, an efficient coupling mechanism becomes

essential. Following Wang et al. (1989) and Wang & Sheeley (1991), large-scale meridional flows have taken up this role (see, e.g., Wang et al. 1991, Choudhuri et al. 1995, Durney 1995, Dikpati & Charbonneau 1999).

In practice, the vast majority of Babcock-Leighton solar cycle models published to date are mean-field-like in that they model the evolution of the large-scale axisymmetric solar magnetic field by solving the $\alpha\Omega$ form of Equations 24 and 25 augmented by an advection term associated with the meridional flow, with all large-scale flows considered to be given (kinematic regime):

$$\frac{\partial A}{\partial t} = \eta \left(\nabla^2 - \frac{1}{\varpi^2} \right) A - \frac{1}{\varpi} \mathbf{u}_p \cdot \nabla(\varpi\, A) + S(r, \theta, B), \tag{40}$$

$$\frac{\partial B}{\partial t} = \eta \left(\nabla^2 - \frac{1}{\varpi^2} \right) B + \frac{1}{\varpi} \frac{d\eta}{dr} \frac{\partial(\varpi\, B)}{\partial r} - \varpi \nabla \cdot \left(\frac{B}{\varpi} \mathbf{u}_p \right)$$
$$+ \varpi (\nabla \times A\hat{\mathbf{e}}_\phi) \cdot (\nabla\Omega), \tag{41}$$

where $\mathbf{u}_p \equiv u_r\hat{\mathbf{e}}_r + u_\theta\hat{\mathbf{e}}_\theta$ (compare with Equations 24 and 25). A mean-field-like turbulent magnetic diffusivity is implicitly invoked, now allowing for a variation with depth, and the novel (nonlinear) source term $S(r, \theta, B)$ appearing on the right-hand side of Equation 40 replaces the α-effect and operates only in the near-surface layers. It is typically formulated as an ad hoc parameterization of the Babcock-Leighton mechanism, required here because a fundamentally nonaxisymmetric process must be "forced" into a global axisymmetric model (see, e.g., Durney 1995, Dikpati & Charbonneau 1999, Nandy & Choudhuri 2001, Chatterjee et al. 2004, Charbonneau et al. 2005, Muñoz-Jaramillo et al. 2010). Most models use a steady meridional flow characterized by a single flow cell per hemisphere, with the flow speed set by the average poleward flow measured at the solar surface (e.g., Hathaway 1996, Ulrich 2010).

As with other flux transport dynamos, equatorward propagation of the internal toroidal field is achieved here through the advective effect of the meridional flow. If the advective terms on the right-hand sides of Equations 40 and 41 dominate over the diffusive terms (the "advection-dominated regime"), then the cycle period is inversely proportional to the meridional flow speed (Wang et al. 1991, Dikpati & Charbonneau 1999). The required (turbulent) magnetic diffusivity values turn out to be two orders of magnitude smaller than estimates based on, e.g., Equation 18 or mixing length theory, but even with larger magnetic diffusivity values (the diffusion-dominated regime), solar-like dynamo solutions are readily obtained (see also Muñoz-Jaramillo et al. 2011). The inclusion of turbulent pumping as an additional contribution to the large-scale flows further improves the solutions, also providing an additional coupling from the surface source region to the base of the convection zone (Guerrero & De Gouveia Dal Pino 2008, Kitchatinov & Olemskoy 2012). With surface poleward flow speeds on the order of 10 m s^{-1}, as observed, reversal of the polar field occurs around the time of cycle maximum, also as observed. However, the associated polar field strengths tend to be much larger than observed, and the deep toroidal field often develops a branch at high latitude associated with the shearing action of the radial shear in the high-latitude reaches of the tachocline. Some of these difficulties can be alleviated by changes in the imposed meridional flow profile, enhanced magnetic diffusivity in the surface layers, and/or inclusion of downward turbulent pumping in the subsurface layers (see, e.g., Dikpati et al. 2004, Jiang et al. 2009, Kitchatinov & Olemskoy 2012). Finally, these dynamo models can in principle operate in the strong-field regime—indeed, they require strong internal toroidal fields to operate.

5.3. Cycle Amplitude Fluctuations and Grand Minima

An appealing property of Babcock-Leighton solar cycle models is their response to fluctuations in the (imposed) meridional flow speed. Many observed features of the sunspot cycles can be
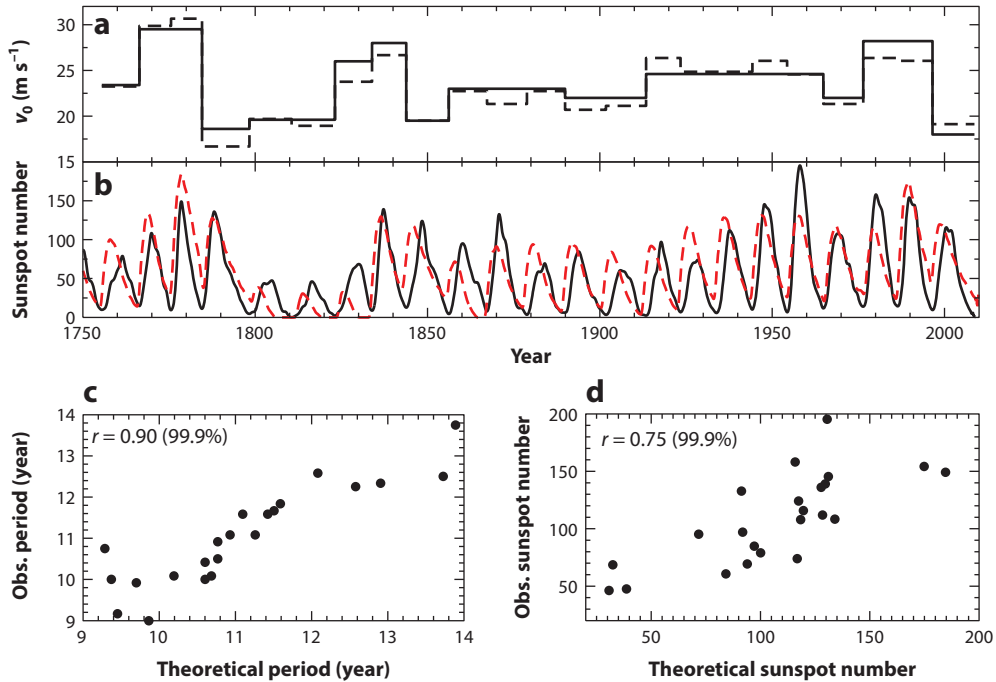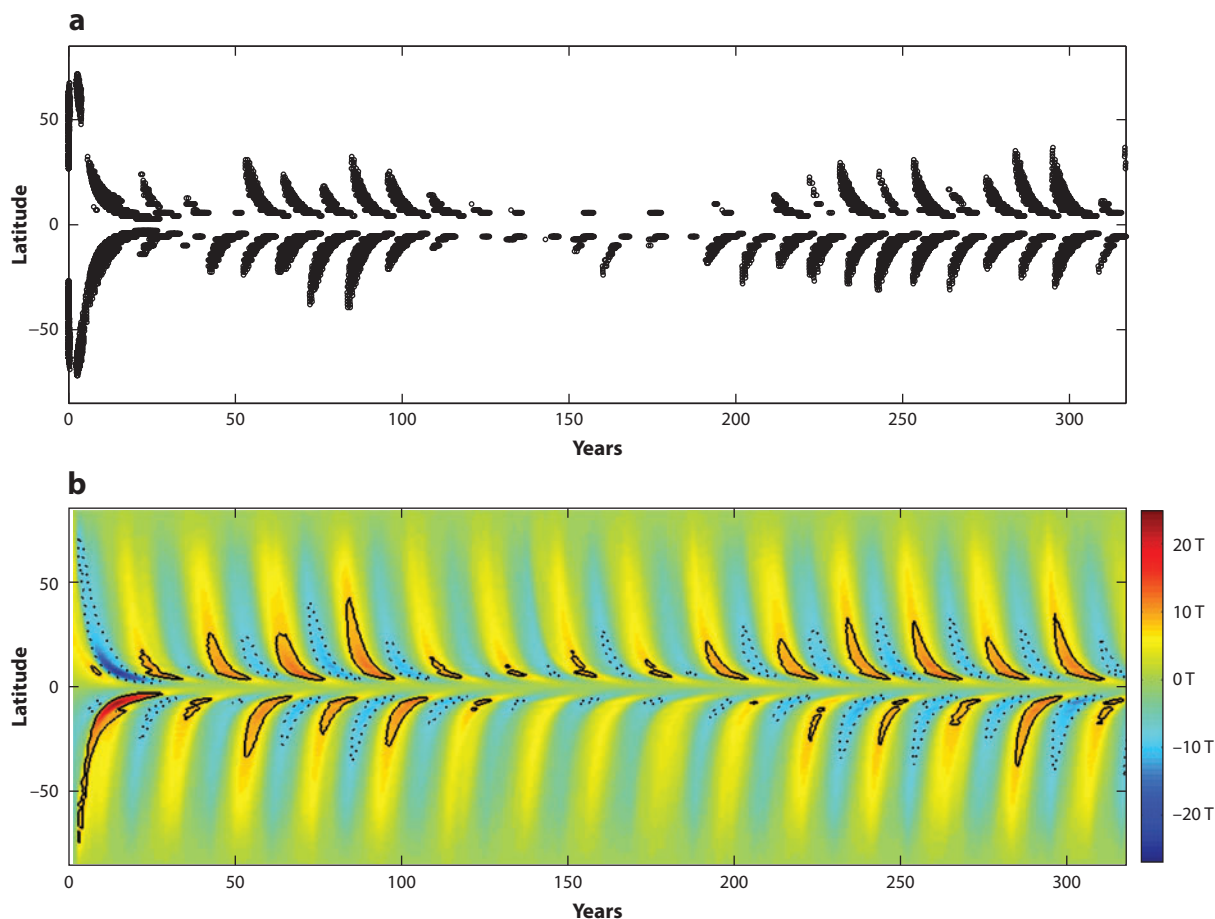
Figure 10

Impact of forced fluctuations of the meridional flow in the kinematic Babcock-Leighton dynamo model by Chatterjee et al. (2004). The (*a*) piecewise-constant imposed meridional flow variations lead to (*b*) a time series of pseudosunspot emergences (*red*) whose (*c*) amplitudes and (*d*) durations correlate quite well with the observed sunspot number time series (*black* in panel *b*). Reproduced from Karak (2010) with permission.

recovered, including the observed relationship between cycle amplitude and period (e.g., Dikpati et al. 2010, Karak & Choudhuri 2011, Nandy et al. 2011). **Figure 10**, taken from Karak (2010) offers a particularly impressive example. Working with the Chatterjee et al. (2004) kinematic model, the meridional flow speed is artificially adjusted from one sunspot cycle to the next as plotted in **Figure 10a**, which leads to the cyclic behavior plotted as a red dashed line in **Figure 10b**. The correlation with the observed sunspot number time series (in *black*) is excellent (e.g., **Figure 10c,d**). This appears to be a robust result in that a similar behavior materializes in other formulations of Babcock-Leighton dynamos (e.g., Passos & Lopes 2008, Lopes & Passos 2009). Another sunspot feature reproduced by such models is the observed alternance between higher-than-average and lower-than-average cycle amplitude, a pattern that can arise naturally from the time delay between poloidal field production at the surface and its shearing by differential rotation upon being transported in the tachocline by the meridional flow (see Charbonneau 2001, Charbonneau et al. 2007 and references therein).

Because the Babcock-Leighton mechanism is characterized by a lower operating threshold on the internal toroidal field strength, the associated dynamo can shut off if the field falls below this threshold in response to perturbations of whatever origin. This feature is also shared by dynamos relying on the instability of magnetic flux tubes in the tachocline, mentioned in Section 4.6. Recovering "normal" cyclic behavior then requires an additional source to kick-start the dynamo once again (see, e.g., Schmitt et al. 1996, Ossendrijver 2000a, Charbonneau et al. 2004). Unlike the nonlinear amplitude modulation of mean-field dynamos discussed in Section 4.7, here the dynamo
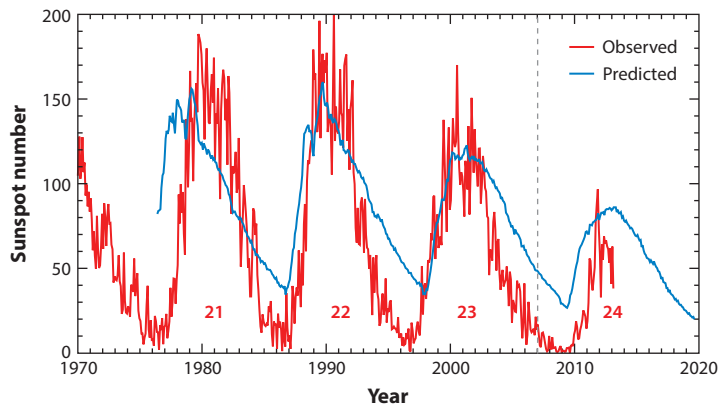
Figure 11

A grand minimum in the stochastically forced kinematic Babcock-Leighton dynamo model by Passos et al. (2014). (*a*) The time-latitude distribution of individual sunspot emergences in the model; (*b*) the time-latitude distribution of the deep toroidal magnetic field giving rise to these emergences. The first ~50 years of these simulations are spent relaxing the initial condition. Note the residual activity during the minimum epoch going from 120 to 200 years and the associated significant north-south asymmetry in emergences. Figure provided by D. Passos (CENTRA/IST).

is switching between two distinct dynamical states, a process known as intermittency. **Figure 11** shows an example taken from Passos et al. (2014). Intermittency is driven here by stochastic forcing of two source terms, one of the Babcock-Leighton type, the other a conventional α-effect operating throughout the convection zone. Similar behavior has also been obtained by simultaneous stochastic forcing of the meridional flow and Babcock-Leighton source term (Choudhuri & Karak 2012).

All of these results are predicated on a meridional flow pattern characterized by a single flow cell per hemisphere. Multiple cells stacked in depth and/or latitude can have a strong impact on the operation of these models (see, e.g., Jouve & Brun 2007). However, recent modeling work suggests that what matters primarily is the presence of an equatorward flow near the base of the convection zone and an efficient mechanism, or combination of mechanisms, to carry the surface magnetic field there (Hazra et al. 2014, Pipin & Kosovichev 2013). Much remains to be learned

Figure 12

Prediction of the timing and amplitude of activity cycle 24 according to the dynamo-based scheme by Choudhuri et al. (2007). The observed monthly sunspot number (SSN) is plotted in red, and the blue curve shows the model's prediction after internal parameter calibration on the 1975–2007 interval. This prediction for cycle 24 was actually made in 2007 (*vertical dotted line*) in the descending phase of cycle 23. The high SSN value at cycle minima is a consequence of the excessive cycle overlap characterizing the underlying dynamo model; it affects the prediction for the timing of cycle minima, but has no impact here on prediction of cycle peak amplitude. Figure produced from numerical data provided by Arnab Rai Choudhuri (IIS, Bangalore).

also on the magnetic backreaction on the meridional flow and how it affects dynamo action in flux transport dynamos in general (Rempel 2006b, Karak & Choudhuri 2012, Passos et al. 2012).

5.4. Cycle Prediction

Because the solar magnetic cycle modulates the frequency of all geoeffective solar eruptive phenomena, prediction of its characteristics is considered an important aspect of space weather forecasting (Petrovay 2010). In Babcock-Leighton dynamo models, the evolving surface magnetic field at cycle n acts as a source of the toroidal field for cycle $n + 1$ after being transported in the interior by the meridional flow. This implies that some prediction of the characteristics of cycle $n + 1$ could be produced from magnetic field observations at cycle n. This idea forms the basis of the so-called precursor methods (see Petrovay 2010, his section 2).

Dikpati et al. (2006) have developed a novel, dynamo-based prediction scheme in which a parameterization of the zonally averaged observed surface magnetic flux is used as a surface boundary condition to a modified Babcock-Leighton model (see also Dikpati & Gilman 2006). **Figure 12** shows a cycle 24 prediction produced by the similar prediction scheme developed by Choudhuri et al. (2007; see also Jiang et al. 2007). Interestingly, these two closely related dynamo-based approaches have led to markedly distinct predictions for cycle 24, indicating that the prediction is sensitive to modeling details (see also Cameron & Schüssler 2007, Bushby & Tobias 2007). Substantial efforts are underway to understand and improve the predictive capabilities of this type of forecasting scheme (e.g., Yeates et al. 2008, Karak & Nandy 2012, Dikpati & Anderson 2012, Muñoz-Jaramillo et al. 2013).

6. CONCLUDING REMARKS

These are very exciting times for solar dynamo theory. The past two decades have witnessed a wide diversification of dynamo mechanisms and solar cycle models, propelled and constrained by the ever more-detailed view of solar internal flows provided by helioseismology and of ever finer

surface magnetic field observations. The subtle role of magnetic helicity in constraining large-scale dynamo action has been recognized and by now largely clarified. In parallel, spectacular advances in computing power and algorithmic design have jointly contributed to the development of global MHD simulations of solar convection and dynamo action, which can reproduce more and more features of the real solar cycle. These represent outstanding virtual laboratories within which physical insight gained from simpler modeling approaches can be tested and validated, and these in turn can guide the design of improved global simulations. Understanding the workings of the solar dynamo remains the ultimate goal, and in this respect the words of computer scientist R.W. Hamming (1962) are as timely now as they were over fifty years ago: "The purpose of computing is insight, not numbers."

FUTURE ISSUES

1. **How critical are subgrid models?** Empirical evidence accumulated to date indicates that this seemingly secondary and highly technical computational issue is actually of great importance for magnetic self-organization. Detailed intercomparison of similar global MHD simulations using distinct subgrid formulations is essential to disentangle which aspects of magnetic self-organization are critically dependent on such computational details.

2. **What sets the dynamo period?** It is sobering to reflect upon the fact that over 150 years after the discovery of the solar cycle, the mechanism(s) setting its period has not yet been pinned down with confidence. In mean-field and mean-field-like models, the possibility to adjust parameter values not well-constrained observationally often makes it possible to obtain solar-like cycle periods no matter which dynamo modeling framework is adopted. This is where observations of magnetic activity cycles in stars other than the Sun can offer powerful discriminants. The importance of sustained monitoring of solar-type stars, such as those carried out by the Mt. Wilson program for decades, cannot be overstated.

3. **Is the tachocline important in driving the dynamo?** Various lines of evidence point to the tachocline as an important agent in achieving magnetic self-organization on large spatial scales. This is a towering computational and physical challenge given the expected strong anisotropy of turbulence therein, the interactions of waves excited by convective overshoot with large-scale flow and magnetic fields, the development of dynamical instabilities, and possible coupling to an underlying fossil magnetic field.

4. **Is the Babcock-Leighton mechanism crucial?** The Babcock-Leighton mechanism is clearly observed to operate at the solar surface; however, it remains unclear whether it represents a mere by-product or an essential element of the dynamo loop. This question may perhaps be answered through an accurate determination of the magnetic flux budget of the solar polar caps, which represents a challenging observational undertaking.

5. **What triggers grand minima?** As reviewed in Sections 4.7 and 5.3, many "simple" mean-field or mean-field-like dynamo models can produce Maunder-Minimum-like episodes of interrupted cyclic behavior, or strongly suppressed magnetic cycle amplitude, through distinct combinations of deterministic and stochastic forcing mechanisms. Most of these scenarios were developed in the context of mean-field or mean-field-like dynamo models, and the hunt is now on to produce similar behavior in dynamically consistent MHD simulations of large-scale magnetic cycles.

DISCLOSURE STATEMENT

ACKNOWLEDGMENTS

LITERATURE CITED

Babcock HW. 1961. *Ap. J.* 133:572–87
Balbus SA, Bonart J, Latter HN, Weiss NO. 2009. *MNRAS* 400:176–82
Barnes G, MacGregor KB, Charbonneau P. 1998. *Ap. J. Lett.* 498:L169–72
Baumann I, Schmitt D, Schüssler M, Solanki SK. 2004. *Astron. Astrophys.* 426:1075–91
Beaudoin P, Charbonneau P, Racine É, Smolarkiewicz PK. 2013. *Solar Phys.* 282:335–60
Beer J. 2000. *Space Sci. Rev.* 94:53–66
Beer J, Tobias SM, Weiss NO. 1998. *Solar Phys.* 181:237–49
Benevolenskaya EE. 1995. *Solar Phys.* 161:1–8
Benevolenskaya EE. 1998. *Ap. J. Lett.* 509:49–52
Berger MA, Field GB. 1984. *J. Fluid. Mech.* 147:133–48
Berger MA, Ruzmaikin A. 2000. *J. Geophys. Res.* 105(A5):10481–90
Blackman EG, Brandenburg A. 2002. *Ap. J.* 579:359–73
Braithwaite J, Nordlund Å. 2006. *Astron. Astrophys.* 450:1077–95
Brandenburg A. 2001. *Ap. J.* 550:824–40
Brandenburg A. 2005. *Ap. J.* 625:539–47
Brandenburg A, Dobler W. 2001. *Astron. Astrophys.* 369:329–38
Brandenburg A, Subramanian K. 2005. *Phys. Rep.* 417:1–209
Brandenburg A, Tuominen I, Nordlund Å, Pulkkinen P, Stein RF. 1990. *Astron. Astrophys.* 232:277–91
Braun DC, Fan Y. 1998. *Ap. J. Lett.* 508:L105–8
Brooke JM, Moss D, Phillips A. 2002. *Astron. Astrophys.* 395:1013–22
Brown BP, Browning MK, Brun AS, Miesch MS, Toomre J. 2010. *Ap. J.* 711:424–38
Brown BP, Miesch MS, Browning MK, Brun AS, Toomre J. 2011. *Ap. J.* 731:69
Browning MK, Miesch MS, Brun AS, Toomre J. 2006. *Ap. J. Lett.* 648:L157–60
Brummell NH, Hurlburt NE, Toomre J. 1996. *Ap. J.* 473:494–513
Brun AS, Miesch MS, Toomre J. 2004. *Ap. J.* 614:1073–98
Brun AS, Miesch MS, Toomre J. 2011. *Ap. J.* 742:79
Bushby PJ. 2006. *MNRAS* 371:772–80
Bushby PJ, Tobias SM. 2007. *Ap. J.* 661:1289–96
Busse FH. 2002. *Phys. Fluids* 14:1301–14
Caligari P, Moreno-Insertis F, Schüssler M. 1995. *Ap. J.* 441:886–902
Cally PS, Dikpati M, Gilman PA. 2003. *Ap. J.* 582:1190–205
Cameron R, Schüssler M. 2007. *Ap. J.* 659:801–11
Cattaneo F. 1999. *Ap. J. Lett.* 515:L39–42
Cattaneo F, Emonet T, Weiss NO. 2003. *Ap. J.* 515:1183–98
Cattaneo F, Hughes DW. 1996. *Phys. Rev. E* 54:4532–35

Cattaneo F, Hughes DW. 2006. *J. Fluid Mech.* 553:401–18

Charbonneau P. 2001. *Solar Phys.* 199:385–404

Charbonneau P. 2010. *Living Rev. Solar Phys.*7:lrsp-2010-3

Charbonneau P. 2013. *Solar and Stellar Dynamos*. Berlin: Springer. 237 pp.

Charbonneau P, Beaubien G, St-Jean C. 2007. *Ap. J.* 658:657–62

Charbonneau P, Blais-Laurier G, St-Jean C. 2004. *Ap. J. Lett.* 616:L183–86

Charbonneau P, MacGregor KB. 1996. *Ap. J. Lett.* 473:L59–62

Charbonneau P, MacGregor KB. 2001. *Ap. J.* 559:1094–107

Charbonneau P, St-Jean C, Zacharias P. 2005. *Ap. J.* 619:613–22

Chatterjee P, Guerrero G, Brandenburg A. 2011. *Astron. Astrophys.* 525:A5

Chatterjee P, Nandy D, Choudhuri AR. 2004. *Astron. Astrophys.* 427:1019–30

Choudhuri AR. 1990. *Ap. J.* 355:733–44

Choudhuri AR, Chatterjee P, Jiang J. 2007. *Phys. Rev. Lett.* 98:131103

Choudhuri AR, Karak BB. 2012. *Phys. Rev. Lett.* 109:171103

Choudhuri AR, Schüssler M, Dikpati M. 1995. *Astron. Astrophys.* 303:L29–32

Clune TL, Elliot JR, Glatzmaier GA, Miesch MS, Toomre J. 1999. *Parallel Comput.* 25:361

Cossette JF, Charbonneau P, Smolarkiewicz PK. 2013. *Ap. J. Lett.* 777:L29

Courvoisier A, Hughes DW, Tobias SM. 2006. *Phys. Rev. Lett.* 96(3):034503

Courvoisier A, Hughes DW, Tobias SM. 2009. *J. Fluid Mech.* 627:403–21

Davidson PA. 2001. *An Introduction to Magnetohydrodynamics*. Cambridge: Cambridge Univ. Press. 431 pp.

de Wijn AG, Stenflo JO, Solanki SK, Tsuneta S. 2009. *Space Sci. Rev.* 144:275–315

Démoulin P, Berger MA. 2003. *Solar Phys.* 215:203–15

Dikpati M, Anderson JL. 2012. *Ap. J.* 756:20

Dikpati M, Cally PS, Gilman PA. 2004. *Ap. J.* 610:597–615

Dikpati M, Charbonneau P. 1999. *Ap. J.* 518:508–20

Dikpati M, de Toma G, Gilman PA. 2006. *Geophys. Res. Lett.* 33:L05102

Dikpati M, Gilman PA. 2001. *Ap. J.* 610:597–615

Dikpati M, Gilman PA. 2006. *Ap. J.* 649:498–514

Dikpati M, Gilman PA, de Toma G, Ulrich RK. 2010. *Geophys. Res. Lett.* 37:L14107

Dikpati M, Gilman PA, Rempel M. 2003. *Ap. J.* 596:680–97

D'Silva S, Choudhuri AR. 1993. *Astron. Astrophys.* 272:621–33

Dubé C, Charbonneau P. 2013. *Ap. J.* 775:69

Durney BR. 1995. *Solar Phys.* 160:213–35

Eddy JA. 1976. *Science* 192(4245):1189–202

Fan Y. 2009. *Living Rev. Solar Phys.* 6:lrsp-2009-4

Fan Y, Fisher GH, DeLuca EE. 1993. *Ap. J.* 405:390–401

Ferriz-Mas A, Schmitt D, Schüssler M. 1994. *Astron. Astrophys.* 289:949–56

Fletcher ST, Broomhall A-M, Salabert D, Basu S, Chaplin WJ, et al. 2010. *Ap. J. Lett.* 718:L19–22

Foukal PF, Fröhlich C, Spruit H, Wigley TML. 2006. *Nature* 443(7109):61–166

Fröhlich C. 2009. *Astron. Astrophys.* 501:L27–30

Fröhlich C, Lean J. 2004. *Astron. Astrophys. Rev.* 12:273–320

Ghizaru M, Charbonneau P, Smolarkiewicz PK. 2010. *Ap. J. Lett.* 715:L133–37

Gilman PA. 1983. *Ap. J. Suppl.* 53:243–68

Gilman PA, Dikpati M, Miesch MS. 2007. *Ap. J. Suppl.* 170:203–27

Gilman PA, Fox PA. 1997. *Ap. J.* 484:439–54

Glatzmaier GA. 1984. *J. Comput. Phys.* 55:461–84

Glatzmaier GA. 1985. *Ap. J.* 291:300–307

Grinstein FF, Margolin LG, Rider WJ, eds. 2007. *Implicit Large Eddy Simulation: Computing Turbulent Fluid Dynamics*. Cambridge: Cambridge Univ. Press. 546 pp.

Guerrero G, de Gouveia Dal Pino EM. 2008. *Ap. J.* 485:267–73

Guerrero G, Smolarkiewicz PK, Kosovichev A, Mansour N. 2013. *Ap. J.* 779:176

Hale GE, Ellerman F, Nicholson SB, Joy AH. 1919. *Ap. J.* 49:153–78

Hamming RW. 1962. *Numerical Methods for Scientist and Engineers*. New York: McGraw-Hill. 721 pp.

Hathaway DH. 1996. *Ap. J.* 460:1027–33

Hathaway DH. 2010. *Living Rev. Solar Phys.* 7:lrsp-2010-1

Hathaway DH. 2012. *Ap. J.* 760:84

Hazra G, Karak BB, Choudhuri AR. 2013. *Ap. J.* 782:93

Howe R. 2009. *Living Rev. Solar Phys.* 6:lrsp-2009-1

Hoyng P. 2003. In *Advances in Nonlinear Dynamos*, ed. A Ferriz-Mas, M Nuñez, pp. 1–36. London: Taylor & Francis

Hoyt DV, Schatten K. 1998. *Solar Phys.* 179:189–219

Hubbard A, Brandenburg A. 2012. *Ap. J.* 748:51

Hubbard A, Del Sordo F, Käpylä P, Brandenburg A. 2009. *MNRAS* 398:1891–99

Hughes DW, Cattaneo F. 2008. *J. Fluid Mech.* 594:445–61

Hughes DW, Proctor MRE, Cattaneo F. 2011. *MNRAS* 414:L45–49

Jiang J, Cameron R, Schmitt D, Isik E. 2013. *Astron. Astrophys.* 553:A128

Jiang J, Cameron R, Schmitt D, Schüssler M. 2009. *Ap. J. Lett.* 693:L96–99

Jiang J, Chatterjee P, Choudhuri AR. 2007. *MNRAS* 381:1527–42

Jouve L, Brun AS. 2007. *Astron. Astrophys.* 474:239–50

Käpylä PJ, Korpi MJ, Brandenburg A. 2009. *Astron. Astrophys.* 500:633–46

Käpylä PJ, Korpi MJ, Brandenburg A, Mitra D, Tavakol R. 2010. *Astron. Nachr.* 331:73

Käpylä PJ, Korpi MJ, Ossendrijver MAJH, Stix M. 2006a. *Astron. Astrophys.* 455:401–12

Käpylä PJ, Korpi MJ, Tuominen I. 2006b. *Astron. Nachr.* 327(9):884–94

Käpylä PJ, Mantere MJ, Brandenburg A. 2012. *Ap. J. Lett.* 755:L22

Käpylä PJ, Mantere MJ, Cole E, Warnecke J, Brandenburg A. 2013. *Ap. J.* 778:41

Karak BB. 2010. *Ap. J.* 724:21021–29

Karak BB, Choudhuri AR. 2011. *MNRAS* 410:1503–12

Karak BB, Choudhuri AR. 2012. *Solar Phys.* 278:137–48

Karak BB, Nandy D. 2012. *Ap. J. Lett.* 761:L13

Kim E-J, MacGregor KB. 2003. *Ap. J.* 588:645–54

Kitchatinov LL, Olemskoy SV. 2012. *Solar Phys.* 276:3–17

Kitchatinov LL, Rüdiger G. 1995. *Astron. Astrophys.* 299:446–52

Kleeorin N, Kuzanyan K, Moss D, et al. 2003. *Astron. Astrophys.* 409:1097–105

Krause F, Rädler K-H. 1980. *Mean-Field Magnetohydrodynamics and Dynamo Theory*. Oxford, UK: Pergamon. 271 pp.

Küker M, Arlt R, Rüdiger G. 1999. *Astron. Astrophys.* 343:977–82

Küker M, Rüdiger G, Schultz M. 2001. *Astron. Astrophys.* 374:301–8

Kusano K, Maeshiro T, Yokoyama T, Sakurai T. 2002. *Ap. J.* 577:501–12

Leighton RB. 1969. *Ap. J.* 156:1–26

Li LH, Sofia S. 2001. *Ap. J.* 549:1204–11

Lopes I, Passos D. 2009. *Solar Phys.* 257:1–12

Low BC. 2001. *J. Geophys. Res.* 106(A11):25141–64

Mason J, Hughes DW, Tobias SM. 2002. *Ap. J. Lett.* 580:L89–92

McCracken KG, Beer J, Steinhilber F, Abreu J. 2013. *Solar Phys.* 286(2):609–27

Miesch MS. 2005. *Living Rev. Solar Phys.* 2:lrsp-2005-1

Miesch MS. 2007. *Ap. J. Lett.* 658:L131–34

Miesch MS, Brun AS, Toomre J. 2006. *Ap. J.* 641:618–25

Miesch MS, Gilman PA, Dikpati M. 2007. *Ap. J. Suppl.* 168:337–61

Miesch MS, Toomre J. 2009. *Annu. Rev. Fluid Mech.* 41:317–40

Moffatt HK. 1978. *Magnetic Field Generation in Electrically Conducting Fluids*. Cambridge: Cambridge Univ. Press. 343 pp.

Moss D, Brooke JM. 2000. *MNRAS* 315:521–33

Muñoz-Jaramillo A, Balmaceda LA, DeLuca EE. 2013. *Phys. Rev. Lett.* 111(4):041106

Muñoz-Jaramillo A, Nandy D, Martens PCH, Yeates AR. 2010. *Ap. J. Lett.* 720:L20–25

Muñoz-Jaramillo A, Nandy D, Martens PCH. 2011. *Ap. J. Lett.* 727:L23–26

Mursula K, Ziegler B, Vilppola JH. 2003. *Solar Phys.* 212:201–7

Nandy D, Choudhuri AR. 2001. *Ap. J.* 551:576–85

Nandy D, Muñoz-Jaramillo A, Martens PCH. 2011. *Nature* 471(7336):80–82

Nelson NJ, Brown BP, Brun AS, Miesch MS, Toomre J. 2011. *Ap. J. Lett.* 739:L38

Nelson NJ, Brown BP, Brun AS, Miesch MS, Toomre J. 2013. *Ap. J.* 762:73

Nelson NJ, Brown BP, Brun AS, Miesch MS, Toomre J. 2014. *Solar Phys.* 289:441–58

Ossendrijver MAJH. 2000a. *Astron. Astrophys.* 359:364–72

Ossendrijver MAJH. 2000b. *Astron. Astrophys.* 359:1205–10

Ossendrijver MAJH. 2003. *Astron. Astrophys. Rev.* 11:287–367

Ossendrijver MAJH, Stix M, Brandenburg A. 2001. *Astron. Astrophys.* 376:713–26

Ossendrijver MAJH, Stix M, Brandenburg A, Rüdiger G. 2002. *Astron. Astrophys.* 394:735–45

Parker EN. 1955a. *Ap. J.* 121:491–507

Parker EN. 1955b. *Ap. J.* 122:293–314

Parker EN. 1979. *Cosmical Magnetic Fields*. Oxford, UK: Clarendon. 858 pp.

Parker EN. 1993. *Ap. J.* 408:707–19

Parnell CE, DeForest CE, Hagenaar HJ, et al. 2009 *Ap. J.* 698:75–82

Passos D, Charbonneau P, Beaudoin P. 2012. *Solar Phys.* 279:1–22

Passos D, Lopes I. 2008. *Ap. J.* 686:1420–25

Passos D, Nandy D, Hazra S, Lopes I. 2014. *Astron. Astrophys.* 563:A18

Petrovay KP. 2010. *Living Rev. Solar Phys.* 7:lrsp-2010-6

Petrovay KP, Kerekes A. 2004. *MNRAS* 351:L59–62

Pipin VV, Kosovichev AG. 2011. *Ap. J.* 738:104

Pipin VV, Kosovichev AG. 2013. *Astron. Astrophys.* 776:36

Pitts E, Tayler RJ. 1985. *MNRAS* 216:139–54

Pouquet A, Frisch U, Leorat J. 1976. *J. Fluid Mech.* 77:321–54

Prusa JM, Smolarkiewicz PK, Wyszogrodzki AA. 2008. *Comp. Fluids* 37:1193–207

Racine É, Charbonneau P, Ghizaru M, Bouchat A, Smolarkiewicz PK. 2011. *Ap. J.* 735:46

Rempel M. 2006a. In *Heliophysics: Plasma Physics of the Local Cosmos*, ed. CJ Schrijver, GL Siscoe, pp. 42–74. Cambridge, UK: Cambridge Univ. Press

Rempel M. 2006b. *Ap. J.* 647:662–75

Rogers TM, Glatzmaier GA. 2006. *Ap. J.* 653:756–64

Rogers TM, MacGregor KB. 2011. *MNRAS* 410:946–62

Rogers TM, MacGregor KB, Glatzmaier GA. 2008. *MNRAS* 387:616–30

Rüdiger G, Elstner D, Ossendrijver MAJH. 2003. *Astron. Astrophys.* 406:15–21

Rüdiger G, Hollerbach R. 2004. *The Magnetic Universe: Geophysical and Astrophysical Dynamos*. Weihheim: Wiley-YCH. 343 pp.

Schmitt D, Schüssler M, Ferriz-Mas A. 1996. *Astron. Astrophys.* 311:L1–4

Schou J, Bogart RS. 1998. *Ap. J. Lett.* 504:L131–34

Schrijver CJ, Title AM, van Ballegooijen AA, Hagenaar HJ, Shine RA. 1997. *Ap. J.* 487:424–36

Schrinner M, Rädler K-H, Schmitt D, Rheinhardt M, Christensen UR. 2007. *Geophys. Astrophys. Fluid Dyn.* 101(2):81–116

Simard C, Charbonneau P, Bouchat A. 2013. *Ap. J.* 768(1):16

Smolarkiewicz PK, Charbonneau P. 2013. *J. Comput. Phys.* 236:608–23

Solanki SK, Inhester B, Schüssler M. 2006. *Rep. Prog. Phys.* 69:563–668

Spruit HC. 1999. *Astron. Astrophys.* 349:189–202

Steenbeck M, Krause F. 1969. *Astron. Nachr.* 291:49–84

Stein RF, Nordlund Å. 2006. *Ap. J.* 642:1246–55

Stix M. 1976. *Astron. Astrophys.* 47:243–54

Strugarek A, Brun AS, Zahn J-P. 2011. *Astron. Astrophys.* 532:A34

Talon S, Kumar P, Zahn J-P. 2002. *Ap. J. Lett.* 574:L175–78

Thibault K, Charbonneau P, Crouch AD. 2012. *Ap. J.* 757:187

Tobias SM. 1996. *Ap. J.* 467:870–80

Tobias SM. 1997. *Astron. Astrophys.* 322:1007–17

Tobias SM, Brummell NH, Clune TL, Toomre J. 2001. *Ap. J.* 549:1183–203

Tobias SM, Cattaneo F, Brummell NH. 2011. *Ap. J.* 728:153

Ulrich RK. 2010. *Ap. J.* 725:658–69

Usoskin IG. 2013. *Living Rev. Solar Phys.* 10:lrsp-2013-1

Usoskin IG, Solanki SK, Kovaltsov GA. 2007. *Astron. Astrophys.* 471:301–9

Vögler A, Schüssler M. 2007. *Astron. Astrophys.* 465:L43–46

Wang Y-M, Nash AG, Sheeley NR Jr. 1989. *Science* 245:712–18

Wang Y-M, Sheeley NR Jr. 1991. *Ap. J.* 375:761–70

Wang Y-M, Sheeley NR Jr, Nash AG. 1991. *Ap. J.* 383:431–42

Warnecke J, Brandenburg A, Mitra D. 2011. *Astron. Astrophys.* 534:A11

Warnecke J, Käpylä P, Mantere MJ, Brandenburg A. 2012. *Solar Phys.* 280:299–319

Yeates AR, Nandy D, Mackay DH. 2008. *Ap. J.* 673:544–56

Yoshimura H. 1975. *Ap. J.* 201:740–48

Zhao J, Bogart RS, Kosovichev AG, Duvall TL Jr, Hartlep T. 2013. *Ap. J. Lett.* 774:L29

Ziegler U, Rüdiger G. 2003. *Astron. Astrophys.* 394:735–45